J. Fluid Mech. (2003), *vol.* 495, *pp.* 385–411.
DOI: 10.1017/S0022112003006360 Printed in the United Kingdom

Axisymmetric wave regimes in viscous liquid film flow over a spinning disk

By G. M. SISOEV[1,2], O. K. MATAR[1] AND C. J. LAWRENCE[1]

[1]Department of Chemical Engineering and Chemical Technology, Imperial College London, London SW7 2AZ, UK

[2]Department of Mechanics and Mathematics, Lomonosov Moscow State University, Moscow, 119992, Russia

(Received 10 September 2002 and in revised form 20 June 2003)

Finite-amplitude capillary waves, which can accompany the axisymmetric flow of a thin viscous film over a rotating disk, are considered. A system of approximate evolution equations for the film thickness and volumetric flow rates in the radial and azimuthal directions is derived, which contains two similarity parameters. In order to inspire confidence in this model, its steady solutions and their linear stability characteristics are compared to those of the full Navier–Stokes equations. Localized equations, which account for the presence of inertial, capillary, centrifugal and Coriolis forces, are obtained via truncation of the approximate system. Periodic solutions of these equations are then determined and found to be similar to those observed experimentally. Our results suggest that the steady quasi-periodic waves with largest amplitude compare well with experimentally observed wave profiles.

1. Introduction

The flow of a thin film over a spinning disk is central to numerous industrial applications ranging from the intensification of heat and mass transfer processes in chemical reactors, spray and atomization, to powder production in metallurgy. Some of these applications, particularly process intensification, require the formation of large-amplitude waves which give rise to a dramatic increase in heat and mass transfer rates (e.g. Aoune & Ramshaw 1999).

Although similar in many respects to the flow of a thin film down a vertical plane, the so-called falling film problem, flow over a spinning disk lends itself more naturally to potential technological exploitation due to the possibility of controlling the local accelerations. These accelerations, however, vary along the radius, which tends to complicate the mathematical modelling of these flows. Moreover, Coriolis forces, which are absent in the falling film problem, must be taken into consideration in the case of a spinning disk. It is perhaps not surprising, therefore, that the falling film problem has received considerably more attention in the literature than flow over a spinning disk; this is particularly true for the computation of finite-amplitude waves. In this paper, we extend the methods and results developed for the falling film problem to model the axisymmetric flow regimes observed to accompany the flow of a thin liquid film over a spinning disk for a wide range of system parameters.

The majority of experimental investigations of flow over a spinning disk have dealt with measurements of the local maximum (wave peak) or the local mean film

thickness. In the first systematic measurements, carried out by Espig & Hoyle (1965), the maximum wave thickness, $\tilde{h}_{max}$, was measured at two radii using a stainless-steel needle that touched the tip of the wave crests. Three typical flow regimes were identified depending on the flow rate. Increasing the flow rate from a small critical value, below which the film splits into rivulets, leads sequentially to a smooth film surface, the formation of axisymmetric waves travelling to the disk periphery and finally to helical waves superimposed on the axisymmetric waves. Measurements were summarized into plots of $\tilde{h}_{max}(\tilde{r}\Omega^2/\nu^2)^{1/3}$ against $2Q_c/\pi\nu\tilde{r}$ where $\tilde{r}$ is the local radius, Ω is the disk angular velocity, ν is the kinematic viscosity and Q_c is the volumetric flow rate. The authors suggested a linear fit with a constant of proportionality equal to 1.3:

$$\tilde{h}_{max} = 1.3\frac{2Q_c}{\pi[\nu(\Omega\tilde{r}^2)^2]^{1/3}}.$$

Charwat, Kelly & Gazley (1972) used infra-red absorption to investigate the flow dynamics. An overhead camera was used to visualize the film surface. They observed that spiral waves unwind in the direction of rotation and are stationary in a frame rotating with the disk. They also showed that the time-averaged film thickness, $\tilde{h}_m$, was, in all cases, less than the value predicted by the Nusselt solution:

$$\tilde{h}_N = \left(\frac{3\nu Q_c}{2\pi\Omega^2\tilde{r}^2}\right)^{1/3}. \tag{1.1}$$

Charwat *et al.* (1972) used the following relation to fit their data for mean film thickness:

$$\frac{\tilde{h}_m}{\tilde{r}} = 1.6\left(\frac{\nu Q_c}{2\pi\Omega^2\tilde{r}^5}\right)^{0.4}.$$

Matsumoto, Saito & Takashima (1973) used a needle to measure the film thickness. Although these authors did not provide descriptions of the different wave regimes, they did present plots of $\tilde{h}\sqrt{\Omega/\nu}$ against $Q_c/(2\pi\tilde{r}^2\sqrt{\nu\Omega})$ where $\tilde{h}$ is the local film thickness; these results were compared with solutions of the stationary flow problem.

Miyasaka (1974*b*) used the dependence of the electrical conductance of the liquid film on its thickness to examine the impact of a falling liquid jet on the surface of the spinning disk. The author observed that the local mean film thickness may either decrease monotonically as a function of the radius or exhibit a local maximum located a few radii downstream of the falling jet.

Butuzov & Puhovoi (1976) used the parameter $\Omega\tilde{r}Q_c/(2\pi\nu\nu_g)$, in which ν_g is the kinematic viscosity of the gas above the film to distinguish four regions along the radius of the disk: the 'inlet' region, the 'first laminar-wave' region, the 'turbulent' region and the 'second laminar-wave' region. The 'first laminar-wave' region was accompanied by the formation of axisymmetric waves; the distance between the waves was found to vary. The 'turbulent' region contained disordered ripples, while the 'second laminar-wave' region occurred near the disk periphery, where the amplitude of the 'turbulent' ripples appearing upstream is damped due to a decrease in the mean film thickness.

Rifert, Barabash & Muzhilko (1982) used an electrical conductance method to show that wave formation occurs downstream of a relatively short inlet region at $Q_c/(2\pi\tilde{r}\nu) > 1.5$. Increasing the flow rate results in the transformation of simple sinusoidal waves to asymmetric waves with sharp fronts, which then break down into small-scale ripples; the measured values of the mean film thickness were about 20%

less than the Nusselt values. The authors used the following formula to fit their data:

$$\tilde{h}_m = 0.65\left(\frac{Q_c \nu}{\Omega^2 \tilde{r}^2}\right)^{1/3}.$$

Using a non-contact capacitance technique, Thomas, Faghri & Hankey (1991) observed wave formation at all values of the flow rate and rotational speed examined. Two wave regimes were distinguished: wavy-laminar and radial-wave (axisymmetric) flows. The former involves irregular wave patterns and the latter occurs at larger values of the rotational speed and is accompanied by the formation of well-defined radially propagating waves travelling on a thin liquid substrate, carrying the main bulk of the liquid to the disk periphery. Their results suggest that the film thickness initially increases with radius up to a local maximum value beyond which it exhibits a monotonic decrease.

Detailed experiments were also carried out by Woods (1995) using an optical technique. Quantitative measurements were obtained through detailed calculation of the reflection and absorption of light passing through a liquid film with a wavy surface. Qualitative information was presented consisting of photographs showing waves on the whole disk and near a given radial position, as well as quantitative data such as average film thickness values at four radial points.

Leneweit, Roesner & Koehler (1999) measured the free-surface velocity and estimated the film thickness by assuming a parabolic radial velocity profile: all of the mean values were found to be less than the Nusselt values. They also found that the spiral waves, generated in the inlet region, are stationary in a laboratory coordinate system, in disagreement with the observation of Charwat *et al.* (1972).

As is clear from the above brief review, many studies have been devoted to determining the characteristics of flow over a spinning disk using a variety of experimental techniques. The majority of these studies, however, have led to what are, essentially, modified versions of the Nusselt formula that have been developed to fit the observations. It is noteworthy that none of these relations contain the surface tension coefficient, σ.

Modelling of the flow over a spinning disk has also received some attention in the literature. Many investigators have calculated the stationary axisymmetric waveless flow in the limit of large Eckman number, $E = \nu/(\Omega H_c^2)$, where H_c is a characteristic film thickness, e.g. Shkadov (1973), Rauscher, Kelly & Cole (1973), Woods (1995).

Steady axisymmetric solutions for finite Eckman numbers have also been obtained in the framework of the boundary layer approximation: Dorfman (1967) used a finite-difference method, Miyasaka (1974*a*) applied the Pohlhausen method. Sisoev, Tal'drik & Shkadov (1986) used a collocation method to allow the computation of steady flows at values of the Eckman number down to unity. Self-similar solutions have been calculated by Lepekhin *et al.* (1981) and Shvets *et al.* (1992).

Modelling studies have also addressed the linear stability characteristics of flow over a spinning disk. Charwat *et al.* (1972) examined the linear stability of the flow in the case of large Eckman numbers in the small wavenumber limit. They found that axisymmetric perturbations have the largest amplification factors and Coriolis forces exert a stabilizing influence. Eliseev (1983), who examined the linear stability of time-periodic perturbations, showed that the wavelength of the perturbation determines the radial domain of the instability, which becomes wider with increasing wavelength. The range of unstable wavenumbers approaches that for the falling film case with increasing radius.

The linear stability of axisymmetric perturbations under conditions of locally uniform flow was analysed by Sisoev & Shkadov (1987) for large Eckman numbers; only the leading-order contributions were considered. A generalized Orr–Sommerfeld problem of sixth order was derived, which contained three similarity parameters. The range of unstable perturbations, which were either spatially or temporally periodic, was computed and neutral stability curves were presented. Sisoev & Shkadov (1990) subsequently extended the analysis to arbitrary Eckman numbers and non-axisymmetric disturbances.

A few studies in the framework of lubrication theory (neglecting the convective inertia terms) have also been devoted to the solution of the nonlinear evolution equations describing the flow over a spinning disk. The first such study, presented by Emslie , Bonner & Peck (1958), spawned many further investigations (see Myers 1998). Also notable is the work of Needham & Merkin (1987), which examined the unsteady flow driven by perturbations applied to the flux. Their linear stability analyses, for large Eckman number in the presence of gravity, g, led to a simple instability criterion in the form $Q_c\Omega^2/2\pi g\nu > 5/6$. However, due to the absence of surface tension from Needham & Merkin's analysis, no large-wavenumber cut-off was obtained.

More recently, the lubrication approach was adopted by Woods (1995) in order to conduct a linear stability analysis of spiral perturbations. Lubrication theory, however, may only be applied to very thin films for which the amplitude of the waves is too small to be observed experimentally. In addition, the Coriolis term in the radial momentum equation arises at the same order as the other inertial terms, which are neglected in the lubrication approximation (Myers & Charpin 2001). Thus, lubrication theory requires the omission of a distinctive feature of the spinning disk problem.

In order to faithfully model the nonlinear wave regimes in flow over a spinning disk, Shkadov (1973) developed a framework to compute these waves at large Eckman number, making use of the falling film solutions. This method was not developed further at that time due to the dearth of experimental data. Moreover, at that time, only the so-called first family of solutions had been calculated for falling films (Shkadov 1967). We have recently applied this approach, taking account of more recent developments in falling film theory, in Sisoev, Matar & Lawrence (2003) to explain some experimental data of Woods (1995) corresponding to large Eckman numbers.

In the present paper, we extend the approach of Shkadov (1973) to the case of finite Eckman number, which is typical of experimental conditions. Thus the model derived below reduces to that used by Shkadov (1967) in the limit of large Eckman numbers and may be used to carry out parametric continuation into the realm of finite Eckman numbers, leading to the computation of solutions that can be compared with experimental observations.

Before proceeding further, however, some issues must be addressed that are common to both falling films and flow over a spinning disk. In the case of a falling film, comparison of model predictions with experimental observations requires knowledge of at least two physical parameters, for instance the wavelength and wave velocity (Shkadov 1967). Another problem arises due to the non-uniqueness of wave solutions for a given set of governing parameters that was first revealed by Bunov, Demekhin & Shkadov (1984). Modelling studies involving the construction of two-parameter manifolds of steady wave solutions by Sisoev & Shkadov (1999) and systematic numerical experiments by Sisoev & Shkadov (1997*a*, *b*) led to the identification of a set of so-called *dominating waves*, which have the greatest wave velocity and largest

peak height. These are attracting wave regimes that are realized independently of the initial conditions and consist of short waves belonging to the first family, long waves of the second family and some waves of intermediate length belonging to families whose classification number depends on the similarity parameter of the problem. These numerical investigations also showed that, in the vicinity of transitions of the dominating waves from one family to another, regimes featuring spatially and temporally doubly periodic waves occur. The discovery of these dominating waves facilitated the explanation by Shkadov & Sisoev (2000) of the transition regimes observed experimentally. It may be expected that similar dominating waves also exist for a film flowing over a spinning disk.

The wave structure for the case of a spinning disk is expected to be more complicated than that for a falling film due to the radial variation of the body force. Nevertheless, our review of previous experimental studies of such flows reveals that quasi-periodic axisymmetric waves do occur in many cases. It will therefore prove fruitful to look for such axisymmetric quasi-periodic solutions. Assesment of the validity of this approach requires knowledge of two wave parameters as mentioned above. To the best of our knowledge, the work of Woods (1995) is the only experimental investigation that provides this information. In the current work, we present qualitative and quantitative comparisons between theoretical results and the experiments of Woods (1995). Qualitative comparisons will also be made with other experimental investigations.

This paper is organized as follows. The full problem statement is formulated in § 2, in which an approximate model is also derived. Steady axisymmetric solutions are considered in § 3. The localized equations, suitable for the calculation of quasi-periodic waves in the vicinity of a chosen radial position, are formulated and the manifold of their solutions is described in § 4. Comparison of the theoretical results with the experiments of Woods (1995) is made in § 5; a discussion, including comparisons with other experimental studies, is presented in § 6. Finally, concluding remarks are provided.

2. Basic equations

We consider a thin Newtonian incompressible liquid film, of kinematic viscosity ν and density ρ, flowing over a solid impermeable disk spinning with angular velocity Ω. A stationary cylindrical coordinate system, $(\tilde{r}, \theta, \tilde{z})$, along with the velocity field $(\tilde{u}_r, \tilde{u}_\theta, \tilde{u}_z)$, is introduced to formulate the mathematical model describing the dynamics of the film bounded by the free surface ($\tilde{z} = \tilde{h}$) and underlying solid substrate ($\tilde{z} = 0$).

The flow is governed by the continuity equation, the Navier–Stokes equations and an appropriate set of boundary conditions: no-slip and no-penetration at the disk surface, the kinematic boundary condition, shear and normal stress balances at the film surface. These equations are rendered dimensionless via the following scaling:

$$\left.\begin{aligned} &\tilde{t} = \frac{Et}{\Omega}, \quad \tilde{r} = R_c \mathrm{e}^x, \quad \tilde{z} = H_c z, \\ &\tilde{u}_r = \frac{\Omega \tilde{r} u}{E}, \quad \tilde{u}_\theta = \Omega \tilde{r}\left(1 + \frac{v}{E}\right), \quad \tilde{u}_z = \frac{\Omega H_c w}{E}, \quad \tilde{h} = H_c h, \quad \tilde{p} = \rho \Omega^2 \tilde{r}^2 p, \end{aligned}\right\} \tag{2.1}$$

where $\tilde{p}$ is the pressure and $\tilde{t}$ is the time. In (2.1), $E \equiv \nu/(\Omega H_c^2)$, represents the Eckman number, while H_c and R_c are the characteristic scales for the film thickness

and radial coordinate. H_c is chosen so that the dimensionless radial flow rate is equal to unity for a given value of R_c under steady conditions:

$$H_c = \left(\frac{\nu Q_c}{2\pi \Omega^2 R_c^2} \right)^{1/3}.$$

Note that this differs from the Nusselt solution $\tilde{h}_N$ (1.1) by a factor of $3^{1/3}$; this scaling is most appropriate for the problem solution. The Nusselt scaling, however, will be used below for comparison of local wave solutions with experimentally observed waves. The observed waves have a characteristic length scale which is much smaller than R_c, so we introduce the following re-scalings:

$$x_\kappa = \frac{x}{\kappa}, \quad t_\kappa = \frac{t}{\kappa}, \quad w_\kappa = \kappa w, \tag{2.2}$$

where κ is a small coefficient that is to be determined. The governing equations and boundary conditions are written in terms of the dimensionless variables defined in (2.1) and (2.2) as

$$\frac{\partial u}{\partial x_\kappa} + \frac{\partial w_\kappa}{\partial z} + 2\kappa u = 0, \tag{2.3a}$$

$$\frac{\partial u}{\partial t_\kappa} + u\frac{\partial u}{\partial x_\kappa} + w_\kappa \frac{\partial u}{\partial z} + \kappa[u^2 - (v+E)^2] = -\varepsilon^2 E^2 \frac{\partial}{\partial x_\kappa}\left(\frac{p}{\varepsilon^2}\right) + \kappa E^2 \left[\frac{\partial^2 u}{\partial z^2} + \frac{\varepsilon^2}{\kappa^2}\left(\frac{\partial^2 u}{\partial x_\kappa^2} + 2\kappa \frac{\partial u}{\partial x_\kappa} \right) \right], \tag{2.3b}$$

$$\frac{\partial v}{\partial t_\kappa} + u\frac{\partial v}{\partial x_\kappa} + w_\kappa \frac{\partial v}{\partial z} + 2\kappa u\,(v+E) = \kappa E^2 \left[\frac{\partial^2 v}{\partial z^2} + \frac{\varepsilon^2}{\kappa^2}\left(\frac{\partial^2 v}{\partial x_\kappa^2} + 2\kappa \frac{\partial v}{\partial x_\kappa} \right) \right], \tag{2.3c}$$

$$\frac{\varepsilon^2}{\kappa^2}\left(\frac{\partial w_\kappa}{\partial t_\kappa} + u\frac{\partial w_\kappa}{\partial x_\kappa} + w_\kappa \frac{\partial w_\kappa}{\partial z} \right) = -E^2 \frac{\partial p}{\partial z} + \kappa E^2 \frac{\varepsilon^2}{\kappa^2}\left(\frac{\partial^2 w_\kappa}{\partial z^2} + \frac{\varepsilon^2}{\kappa^2}\frac{\partial^2 w_\kappa}{\partial x_\kappa^2} \right), \tag{2.3d}$$

$$z = 0: \quad u = 0, \quad v = 0, \quad w_\kappa = 0, \tag{2.3e–g}$$

$$z = h(x_\kappa, t_\kappa): \quad \frac{\partial h}{\partial t_\kappa} + u\frac{\partial h}{\partial x_\kappa} = w_\kappa, \tag{2.3h}$$

$$p - 2\kappa \frac{\varepsilon^2}{\kappa^2}\left[1 + \left(\frac{\varepsilon}{\kappa}\frac{\partial h}{\partial x_\kappa} \right)^2 \right]^{-1} \left\{ \frac{\partial w_\kappa}{\partial z} - \frac{\partial h}{\partial x_\kappa}\frac{\partial u}{\partial z} + \frac{\varepsilon^2}{\kappa^2}\frac{\partial h}{\partial x_\kappa}\left[\frac{\partial h}{\partial x_\kappa}\left(\kappa u + \frac{\partial u}{\partial x_\kappa} \right) - \frac{\partial w_\kappa}{\partial x_\kappa} \right] \right\} + \frac{1}{We}\frac{\varepsilon^2}{\kappa^2}\left[1 + \left(\frac{\varepsilon}{\kappa}\frac{\partial h}{\partial x_\kappa} \right)^2 \right]^{-3/2} \left[\frac{\partial^2 h}{\partial x_\kappa^2} + \kappa \frac{\varepsilon^2}{\kappa^2}\left(\frac{\partial h}{\partial x_\kappa} \right)^3 \right] = 0, \tag{2.3i}$$

$$\frac{\partial u}{\partial z} + \frac{\varepsilon^2}{\kappa^2}\left[\frac{\partial w_\kappa}{\partial x_\kappa} + 2\frac{\partial h}{\partial x_\kappa}\left(\frac{\partial w_\kappa}{\partial z} - \frac{\partial u}{\partial x_\kappa} - \kappa u \right) - \left(\frac{\partial h}{\partial x_\kappa} \right)^2 \frac{\partial u}{\partial z} \right] - \frac{\varepsilon^4}{\kappa^4}\left(\frac{\partial h}{\partial x_\kappa} \right)^2 \frac{\partial w_\kappa}{\partial x_\kappa} = 0, \tag{2.3j}$$

$$\frac{\partial v}{\partial z} - \frac{\varepsilon^2}{\kappa^2}\frac{\partial h}{\partial x_\kappa}\frac{\partial v}{\partial x_\kappa} = 0. \tag{2.3k}$$

Equations (2.3) incorporate two dimensionless parameterizing functions,

$$We(\tilde{r}) \equiv \frac{\rho \Omega^2 \tilde{r}^2 H_c}{\sigma}, \quad \varepsilon(\tilde{r}) \equiv \frac{H_c}{\tilde{r}},$$

which correspond to the local Weber number, We, in which σ denotes surface tension, and the local aspect ratio, ε, respectively.

We will analyse the case in which

$$\frac{\varepsilon^2}{\kappa^2} \ll 1, \tag{2.4}$$

which reflects the relationship between the two relevant length scales: the wavelength scale, κR_c, is larger than the film thickness, H_c. This relationship is typical for capillary waves induced by a body force directed along the solid substrate. The terms of $O(\varepsilon^2/\kappa^2)$ in (2.3), except the capillary term in the dynamic boundary condition at the free surface, which contains the multiplier $\varepsilon^2/(\kappa^2 We)$, are omitted to obtain a system of equations that is similar to the boundary layer equations but contains the so-called self-induced capillary pressure. Following Shkadov (1967), we choose κ by demanding a balance between the capillary forces and viscous stresses, which is typical for capillary waves in viscous liquid films. Then from the radial component of the Navier–Stokes equations (2.3) it follows that

$$\frac{(\varepsilon\,(R_c))^2}{\kappa^2 We\,(R_c)} = \kappa \qquad \text{or} \qquad \kappa = \left(\frac{(\varepsilon\,(R_c))^2}{We\,(R_c)}\right)^{1/3} = \left(\frac{\sigma H_c}{\rho \Omega^2 R_c^4}\right)^{1/3}. \tag{2.5}$$

The role of inertial forces depends on the parameter κE^2. If this parameter is large, inertial terms can be neglected and the lubrication approximation for very thin films can be applied (Myers & Charpin 2001). In the opposite case, $\kappa E^2 \ll 1$, the film is thick and roll waves would be expected to form. For the experimental conditions discussed below, the viscous, capillary and inertial forces are of the same order.

After omitting terms of $O(\varepsilon^2/\kappa^2)$ in (2.3), the vertical component of the momentum equation and the normal stress balance at the film surface determine that the pressure is constant across the film thickness and arises solely due to capillarity. Consequently, the approximate model can be expressed in the form

$$\frac{\partial u}{\partial x_\kappa} + \frac{\partial w_\kappa}{\partial z} + 2\kappa u = 0, \tag{2.6a}$$

$$\frac{\partial u}{\partial t_\kappa} + u\frac{\partial u}{\partial x_\kappa} + w_\kappa \frac{\partial u}{\partial z} + \kappa(u^2 - v^2) = \frac{1}{45\delta}\left[\exp(-2\kappa x_\kappa)\frac{\partial}{\partial x_\kappa}\left(\exp(-2\kappa x_\kappa)\frac{\partial^2 h}{\partial x_\kappa^2}\right) + \frac{\partial^2 u}{\partial z^2} + 1 + \frac{2v}{E}\right], \tag{2.6b}$$

$$\frac{\partial v}{\partial t_\kappa} + u\frac{\partial v}{\partial x_\kappa} + w_\kappa \frac{\partial v}{\partial z} + 2\kappa u v = \frac{1}{45\delta}\left(\frac{\partial^2 v}{\partial z^2} - \frac{2u}{E}\right), \tag{2.6c}$$

$$z = 0: \quad u = 0, \quad v = 0, \quad w_\kappa = 0, \tag{2.6d–f}$$

$$z = h(x_\kappa, t_\kappa): \quad \frac{\partial h}{\partial t_\kappa} + u\frac{\partial h}{\partial x_\kappa} = w_\kappa, \quad \frac{\partial u}{\partial z} = 0, \quad \frac{\partial v}{\partial z} = 0, \tag{2.6g–j}$$

in which the similarity parameter, δ, is given by

$$\delta \equiv \frac{1}{45\nu^2}\left(\frac{\rho\Omega^8 R_c^4 H_c^{11}}{\sigma}\right)^{1/3}. \tag{2.7}$$

This parameter was first introduced for the falling film problem by Shkadov (1977), where the acceleration due to gravity g replaces the centrifugal acceleration $\Omega^2 R_c$ in (2.7).

The significance of the various dimensionless parameters may be interpreted using the parameter

$$\gamma = \frac{\sigma}{\rho\sqrt{\nu^3\Omega}}$$

which is determined by the liquid properties, ρ, ν and σ, and the angular velocity Ω, and does not depend on either the flow rate or the radial scale. The parameter γ may be termed the Kapitza number for film flow over a spinning disk; the Kapitza number for a falling film is $Ka = \sigma/(\rho(g\nu^4)^{1/3})$ (Kapitza 1948). Then the original parameters may be expressed through the similarity parameters in the form

$$We\,(R_c) = (45\delta)^{3/2}\,E^{9/4}\gamma^{-1/2}, \quad \varepsilon = (45\delta)^{-3/4}\,E^{-15/8}\gamma^{-1/4}.$$

The terms omitted in (2.6) in comparison with (2.3) have the order

$$\frac{\varepsilon^2}{\kappa^2} = (45\delta)^{1/2}\,E^{1/4}\gamma^{-1/2}.$$

The parameter γ is large for most of the experiments reported in the literature; for instance, $\gamma \in (6250, 15300)$ for the experiments, carried out by Woods (1995). As result, relation (2.4) is fulfilled and the approximate model, described by (2.6), depends on just two governing parameters: δ and E, with $\kappa = \left(45\delta E^2\right)^{-1}$.

An integral approximation, or so-called Pohlhausen technique, is employed to derive a system of evolution equations for the film flow. We follow Shkadov (1967) and Demekhin & Shkadov (1984), where the three-dimensional model for the falling film was formulated, and assume that the velocity components have the following profiles:

$$u\,(x_\kappa, z, t_\kappa) = \frac{3q^{(u)}}{h}\left(\frac{z}{h} - \frac{z^2}{2h^2}\right), \quad v\,(x_\kappa, z, t_\kappa) = \frac{5q^{(v)}}{4h}\left(\frac{2z}{h} - \frac{z^3}{h^3} + \frac{z^4}{4h^4}\right), \tag{2.8}$$

where $q^{(u)}$ and $q^{(v)}$ are the flow rates in the radial and tangential directions, respectively:

$$q^{(u)} \equiv \int_0^h u\,\mathrm{d}z, \quad q^{(v)} \equiv \int_0^h v\,\mathrm{d}z.$$

The approximations (2.8) may be considered as an application of the Galerkin method with a single functions for velocity components. This approximation can be verified by direct comparison of the results with experimental data, as is done below. As will also be shown below, the approximation (2.8) gives rise to the Nusselt solution at large Eckman number. Furthermore, Alekseenko, Nakoryakov & Pokusaev (1992) have verified experimentally that the parabolic velocity profile provides a good approximation for falling films for moderate Reynolds numbers.

Integration of (2.6) across the film thickness, followed by substitution of (2.8) yields the following system:

$$\frac{\partial h}{\partial t_\kappa} + \frac{\partial q^{(u)}}{\partial x_\kappa} + 2\kappa q^{(u)} = 0, \tag{2.9a}$$

$$\frac{\partial q^{(u)}}{\partial t_\kappa} + \beta_{11}\frac{\partial}{\partial x_\kappa}\left(\frac{\left(q^{(u)}\right)^2}{h}\right) + \frac{\kappa}{h}\left[\beta_{12}\left(q^{(u)}\right)^2 - \beta_{13}\left(q^{(v)}\right)^2\right] = \frac{1}{45\delta}\left[\exp(-2\kappa x_\kappa)h\frac{\partial}{\partial x_\kappa}\left(\exp(-2\kappa x_\kappa)\frac{\partial^2 h}{\partial x_\kappa^2}\right) - \beta_{14}\frac{q^{(u)}}{h^2} + h + \frac{2q^{(v)}}{E}\right], \tag{2.9b}$$

$$\frac{\partial q^{(v)}}{\partial t_\kappa} + \beta_{21}\frac{\partial}{\partial x_\kappa}\left(\frac{q^{(u)}q^{(v)}}{h}\right) + \beta_{22}\frac{\kappa q^{(u)}q^{(v)}}{h} = -\frac{1}{45\delta}\left(\beta_{23}\frac{q^{(v)}}{h^2} + \frac{2q^{(u)}}{E}\right), \tag{2.9c}$$

with the coefficients given by:

$$\beta_{11} = \tfrac{6}{5}, \quad \beta_{12} = \tfrac{18}{5}, \quad \beta_{13} = \tfrac{155}{126}, \quad \beta_{14} = 3,$$
$$\beta_{21} = \tfrac{17}{14}, \quad \beta_{22} = \tfrac{34}{7}, \quad \beta_{23} = \tfrac{5}{2}.$$

It is important to note that we have retained the $O(\kappa)$ terms in (2.9). These terms represent effects which distinguish the flow over a rotating disk from that in a falling film: the Coriolis forces and radial variation of the local flow rate and of the body force. For given liquid properties, flow rate and angular velocity, the parameters in (2.9) vary with R_c according to $\kappa \sim R_c^{-14/9}$, $\delta^{-1} \sim R_c^{10/9}$ and $(\delta E)^{-1} \sim R_c^{-2/9}$. Thus, the significance of the Coriolis terms decreases with the radius and the system reduces to the two-dimensional falling film model, as applied by Shkadov (1973).

Below, we present three types of solutions to (2.9). First, 'waveless' flows are discussed, and compared with solutions of the thin layer model, (2.6). Linear stability analyses of the waveless solutions of (2.9) and of the full Navier–Stokes problem, (2.3), are then carried out. The purpose of these analyses is to demonstrate the suitability of (2.9) as a good approximation of the full problem. Local nonlinear regular waves are then computed, as approximate solutions of (2.9), and compared with experimental observations.

3. Steady flows

Here, we present steady solutions of (2.9) and compare these results with the solutions of the thin-layer model (2.6). We consider the case for which spatial derivatives arise to leading order. For $\kappa \ll 1$, the first term on the right-hand side of (2.9*b*) is omitted. This corresponds to solutions that are smoothly varying in the radial direction and are not influenced by capillarity. The continuity equation is then solved trivially and we have a system of ordinary differential equations in terms of the original dimensionless variable x:

$$\left.\begin{aligned} &q^{(u)} = \mathrm{e}^{-2x}, \\ &\beta_{11}\frac{\mathrm{d}}{\mathrm{d}x}\left(\frac{\left(q^{(u)}\right)^2}{h}\right) + \beta_{12}\frac{\left(q^{(u)}\right)^2}{h} - \beta_{13}\frac{\left(q^{(v)}\right)^2}{h} = E^2\left(h - \beta_{14}\frac{q^{(u)}}{h^2}\right) + 2Eq^{(v)}, \\ &\beta_{21}\frac{\mathrm{d}}{\mathrm{d}x}\left(\frac{q^{(u)}q^{(v)}}{h}\right) + \beta_{22}\frac{q^{(u)}q^{(v)}}{h} = -\beta_{23}E^2\frac{q^{(v)}}{h^2} - 2Eq^{(u)}. \end{aligned}\right\} \tag{3.1}$$

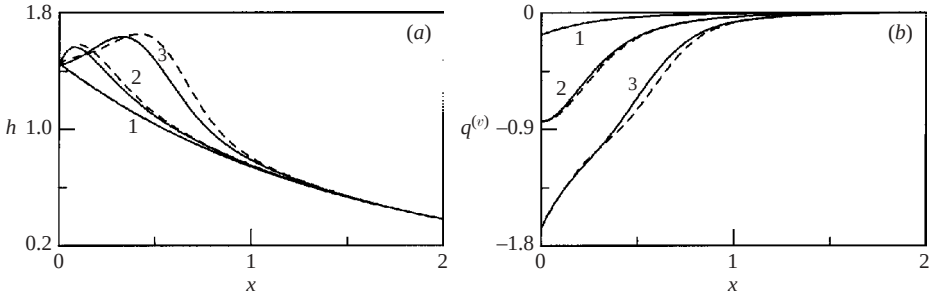

FIGURE 1. (*a*) Film thickness h and (*b*) tangential flow rate $q^{(v)}$ for waveless flows at $E = 10$ (curves 1), $E = 2$ (curves 2), $E = 1$ (curves 3). Solutions of the approximate model, (3.1) (solid curves), and the thin layer approximation, (2.6) (dashed curves), are compared.

Note that the inlet condition $q^{(u)}(0)$ has been chosen so that the dimensional flow rate is equal to Q_c at $\tilde{r} = R_c$. Equations (3.1) must be complemented with appropriate inlet conditions for the film thickness and tangential flow rate, $h(0)$ and $q^{(v)}(0)$, respectively.

For large Eckman numbers, asymptotic solutions of (3.1) may be constructed in the form (Shkadov 1973)

$$h = h_0 + E^{-2}h_1 + \ldots, \quad q^{(v)} = E^{-1}\left(q_0^{(v)} + E^{-2}q_1^{(v)} + \ldots\right). \tag{3.2}$$

The leading-order solutions are given by

$$h_0 = (3\mathrm{e}^{-2x})^{1/3}, \quad q_0^{(v)} = -\frac{4}{15}h_0^5 \tag{3.3}$$

(in which the explicit values of β_{14} and β_{23} have been used). Note that the same leading-order solutions could have been obtained by asymptotic solution of (2.6) in the form

$$\left.\begin{aligned} u = u_0 + E^{-2}u_1 + \ldots, \quad v = E^{-1}(v_0 + E^{-2}v_1 + \ldots), \\ w = w_0 + E^{-2}w_1 + \ldots, \quad h = h_0 + E^{-2}h_1 + \ldots, \end{aligned}\right\} \tag{3.4}$$

which yields the Nusselt solution:

$$\begin{aligned} u_0 &= h_0 z - \frac{z^2}{2}, \quad v_0 = -\frac{2h_0^3}{3}z + \frac{h_0}{3}z^3 - \frac{z^4}{12}, \\ w_0 &= \frac{z^3}{3} - \frac{2h_0}{3}z^2, \quad h_0 = (3\mathrm{e}^{-2x})^{1/3}. \end{aligned} \tag{3.5}$$

Thus, at large Eckman number, the steady solution of the approximation equations (2.9) is the same as that of the thin-layer equations (2.6). The higher-order terms of the series (3.4) are given by Shkadov (1973).

In order to assess the predictions of the approximate system (2.9) at finite Eckman number, we compare its steady solutions, i.e. solutions of (3.1), with steady solutions of (2.6), computed by the method developed by Sisoev *et al.* (1986). This comparison is illustrated in figure 1, which shows solutions of both systems, (2.6) and (3.1), for different values of E. The inlet conditions used correspond to the leading-order terms (3.3) and (3.5) in the respective systems, evaluated at $x = 0$. Figure 1 reveals that both solutions are in close agreement with the Nusselt solution for $E = 10$. A decrease in E, and the concomitant increase in the significance of the nonlinear terms in the governing equations, leads to deviations from the Nusselt solution in the inlet region. Agreement with the Nusselt solution is recovered beyond a certain value of x, which

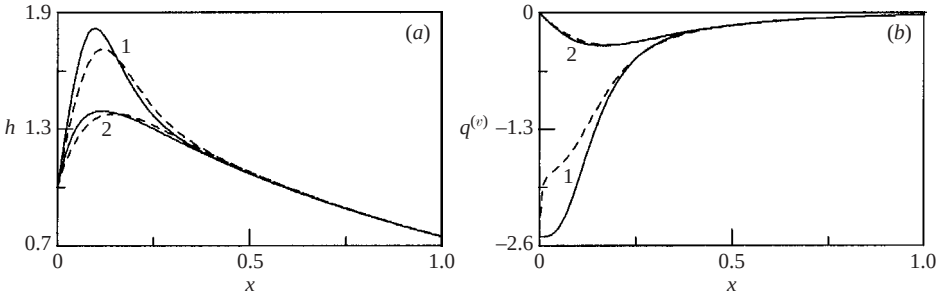

FIGURE 2. (*a*) Film thickness h and (*b*) tangential flow rate $q^{(v)}$ for waveless flows at $E = 2.5$, $h(0) = 1$, $u(0, z) = 0.5\pi \sin(0.5\pi z)$. Two cases of inlet tangential velocity are shown: initially non-rotating liquid with $v(0, z) = -E$ (curves 1) and liquid rotating with the disk $v(0, z) = 0$ (curves 2). Solutions of the approximate model (3.1) (solid curves) and the thin layer approximation (2.6*a*) (dashed curves) are compared.

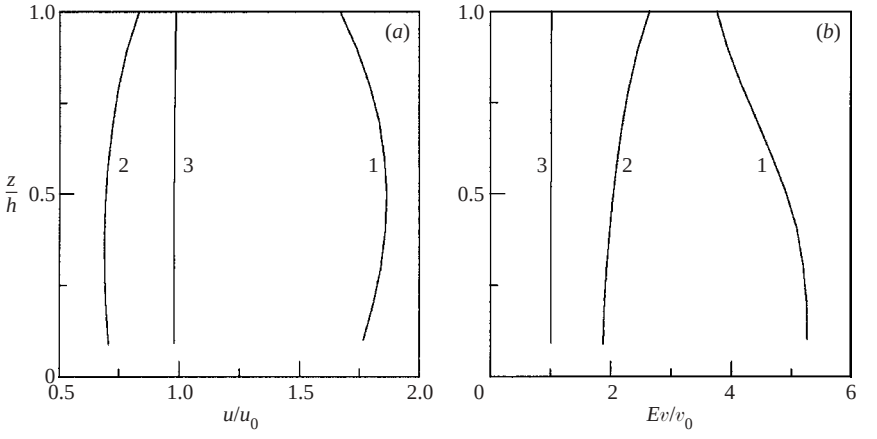

FIGURE 3. Comparison of (*a*) radial and (*b*) tangential velocities computed using (2.6) with the asymptotic forms given in (3.5). The ratio of these velocities is plotted for waveless flow with $E = 2.5$, $h(0) = 1$, $u(0, z) = 0.5\pi \sin(0.5\pi z)$, $v(0, z) = -E$: at $x = 0.01$ (curve 1), $x = 0.1$ (curve 2), $x = 0.5$ (curve 3).

increases with decreasing E. The approximation system (3.1) shown by solid lines gives good quantitative agreement with the more accurate thin-layer equations (2.6) shown by dashed lines.

Further comparisons are shown in figure 2, in which solutions are presented starting from inlet conditions that correspond to a non-parabolic radial velocity profile and two uniform extreme tangential velocity profiles: non-rotating, $v(0, z) = -E$, and rigid body rotation, $v(0, z) = 0$. Close agreement between the solutions of (2.6) and (3.1) is once again demonstrated, except for small x–values in the case where the liquid is initially non-rotating. In the latter case, the solutions for $q^{(v)}$ initially diverge, because the shape of the velocity profile in the solution of (2.6) evolves rapidly at small x. Thereafter the solutions begin to converge and good agreement is found for $x > 0.2$. The comparisons shown in figures 1 and 2 provide good evidence for the validity of the adopted model, which is based on the approximate radial and tangential velocity profiles given by (2.8).

The validity of the assumed forms for the velocity profiles (2.8) is further assessed in figure 3. A direct comparison is shown of the velocity profiles computed using (2.6)

at finite Eckman number and profiles (3.5), which correspond to the leading terms of the asymptotic solution. It is clear that the velocity profile rapidly adjusts to the asymptotic form, since the ratios of the solutions of (2.6) to the asymptotic profiles from (3.5), u/u_0 and Ev/v_0, achieve values very close to unity after a relatively short distance in x. Furthermore, the ratios u/u_0, Ev/v_0 are almost uniform in z, even for very small values of x, which indicates that the assumed shapes of the velocity profiles given in (2.8) are reasonable.

4. Waves

4.1. *Localized equations*

As described in the Introduction of this work, there is considerable experimental evidence for the existence of quasi-periodic waves whose velocity and amplitude are only weakly dependent on the radial coordinate. In order to determine locally periodic solutions of (2.9), the last term in (2.9*a*), as well as the exponential multipliers in the first term on the right-hand side of (2.9*b*) must be omitted. These terms determine the weak dependence of the solutions on the coordinate x_κ.

It is now convenient to reintroduce the factors of 3 from the Nusselt scaling as follows:

$$\left.\begin{aligned} &t'_\kappa = 3^{-4/9}t_\kappa, \quad x'_\kappa = 3^{-1/9}x_\kappa, \quad h' = 3^{-1/3}h, \quad q' = q^{(u)}, \quad p' = 3^{-1/2}q^{(v)}, \\ &\delta' = 3^{11/9}\delta, \quad E' = 3^{-1/6}E, \quad \kappa' = 3^{1/9}\kappa = [15\delta'(E')^2]^{-1}. \end{aligned}\right\} \tag{4.1}$$

The resulting equations can then be written in the form

$$\frac{\partial h}{\partial t_\kappa} + \frac{\partial q}{\partial x_\kappa} = 0, \tag{4.2a}$$

$$\frac{\partial q}{\partial t_\kappa} + \frac{6}{5}\frac{\partial}{\partial x_\kappa}\left(\frac{q^2}{h}\right) + \frac{\kappa}{h}(\beta_{12}q^2 - 3\beta_{13}p^2) = \frac{1}{5\delta}\left(h\frac{\partial^3 h}{\partial x_\kappa^3} + h - \frac{q}{h^2} + \frac{2p}{E}\right), \tag{4.2b}$$

$$\frac{\partial p}{\partial t_\kappa} + \beta_{21}\frac{\partial}{\partial x_\kappa}\left(\frac{pq}{h}\right) + \beta_{22}\frac{\kappa pq}{h} = -\frac{1}{15\delta}\left(\beta_{23}\frac{p}{h^2} + \frac{2q}{E}\right), \tag{4.2c}$$

where the primes have been suppressed here and throughout the remainder of this section. They will be restored in later sections to avoid any ambiguity in comparison with experiments. The transformations (4.1) and substitution of explicit values of β_{11} and β_{14} have been used to emphasize the relationship of these equations to the falling film model of Shkadov (1967). The latter model consists of (4.2*a*, *b*) in the limit of large Eckman number E (and hence small κ).

The equations (4.2) are henceforth referred to as *the localized evolution equations.* Their validity may be tested by comparing the stability properties of (4.2) with the full system of equations (2.3).

The system (4.2) has a stationary solution, $h = H$, $q = Q$, $p = P$, with

$$Q = 1, \quad \frac{\beta_{12} - 3\beta_{13}P^2}{3E^2H} = H - \frac{1}{H^2} + \frac{2P}{E}, \quad \frac{\beta_{22}P}{E^2H} + \frac{\beta_{23}P}{H^2} + \frac{2}{E} = 0. \tag{4.3}$$

Numerical solutions of (4.3) are shown in figure 4. As suggested by figure 1, decreasing E leads locally to an increase in the film thickness and a retardation of the mean azimuthal liquid velocity in comparison with that of the disk. These results demonstrate the significant 'braking' effect of the Coriolis terms. In order

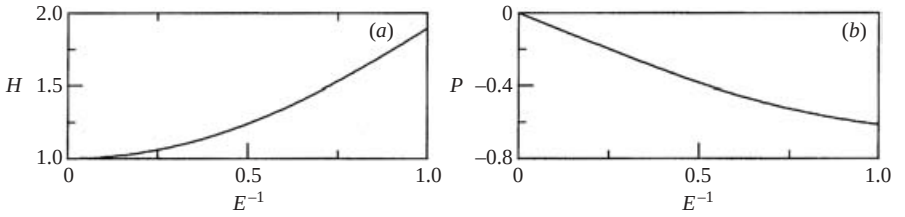

FIGURE 4. (*a*) Film thickness and (*b*) tangential flow rate of the stationary flow (4.3).

to compare the computed nonlinear waves with the finite-amplitude waves observed experimentally by Woods (1995), we will consider primarily the interval $E \geqslant 2$ in which quasi-periodic waves were observed in the experiments.

4.2. *Linear stability analysis*

In order to investigate the linear stability of the basic state, given by the solution of (4.3), we seek solutions of (4.2) of the following normal-mode form:

$$(h, q, p) = (H, Q, P) + (\hat{h}, \hat{q}, \hat{p}) \exp[\mathrm{i}\alpha_\kappa (x_\kappa - c_\kappa t_\kappa)],$$

where the quantities with hats represent small perturbations; α_κ is the real wavenumber and c_κ is the complex phase velocity, the complex frequency is $\omega_\kappa = \alpha_\kappa c_\kappa$. Linearization of (4.2) gives rise to the following eigenvalue equation:

$$\alpha_\kappa^2 c_\kappa^3 + (D_{22} + D_{33})\mathrm{i}\alpha_\kappa c_\kappa^2 + (\mathrm{i}\alpha_\kappa D_{21} + D_{23}D_{32} - D_{22}D_{33})c_\kappa + D_{31}D_{23} - D_{21}D_{33} = 0, \tag{4.4}$$

where

$$D_{21} = -\frac{6\mathrm{i}\alpha_\kappa}{5H^2} + \frac{1}{5\delta}\left(\mathrm{i}\alpha_\kappa^3 H - 1 - \frac{2}{H^3}\right) - \frac{\kappa}{H^2}(\beta_{12} - 3\beta_{13}P^2),$$

$$D_{22} = \frac{12\mathrm{i}\alpha_\kappa}{5H} + \frac{1}{5\delta H^2} + \frac{2\kappa\beta_{12}}{H}, \quad D_{23} = -\frac{6\beta_{13}\kappa P}{H} - \frac{2}{5\delta E},$$

$$D_{31} = -\frac{\mathrm{i}\alpha_\kappa \beta_{21} P}{H^2} - \frac{\beta_{22}\kappa P}{H^2} - \frac{2\beta_{23}P}{15\delta H^3}, \quad D_{32} = \frac{\mathrm{i}\alpha_\kappa \beta_{21} P}{H} + \frac{\beta_{22}\kappa P}{H} + \frac{2}{15\delta E},$$

$$D_{33} = \frac{\beta_{22}\kappa}{H} + \frac{\beta_{23}}{15\delta H^2} + \frac{\mathrm{i}\alpha_\kappa \beta_{21}}{H}.$$

The dependence of the neutral wavenumber $\alpha_{\kappa,n}$ on the similarity parameter δ is shown in figure 5(*a*) for different Eckman numbers. The unstable region is to the left of curves 1–5 or above curves 6–8. For $E^{-1} \leqslant 0.4$, wavelengths longer than $2\pi/\alpha_{\kappa,n}$ are unstable. At infinite Eckman number (curve 1), the neutral value is $\alpha_{\kappa,n} = \sqrt{15\delta}$ (Shkadov 1967). Decreasing the Eckman number leads to a reduction in the band of unstable wavenumbers, as can be seen from curves 2–5. There is a critical Eckman number, with $E^{-1} \in (0.4, 0.41)$, below which the neutral curve is changed significantly: long waves become stable so that there is a small (as well as a large) wavenumber cut-off (see curves 6, 7 and 8 in figure 5*a*). This may be attributed to the stabilizing influence of the Coriolis terms.

In addition to examining the neutral wavenumbers, the frequencies of neutral perturbations $\omega_{\kappa,n} = \alpha_{\kappa,n} c_{\kappa,n}$, are shown in figure 5(*b*). If the stability problem is considered for time-periodic perturbations, then disturbances having frequencies to the left of curves 1–5 or above curves 6, 7, 8 would be unstable and grow downstream.

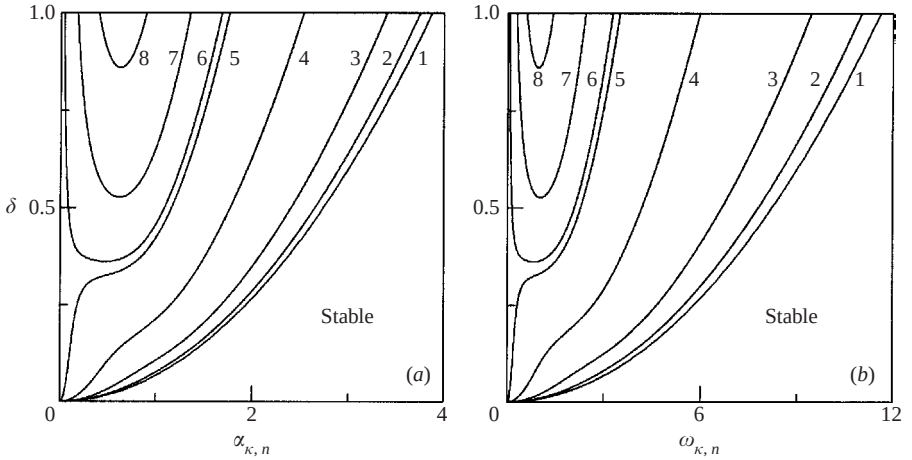

FIGURE 5. (*a*) Neutral wavenumber $\alpha_{\kappa,n}$ and (*b*) neutral frequency $\omega_{\kappa,n}$ as functions of the parameter δ. Curves 1–8 were generated with $E^{-1} = 0, 0.1, 0.2, 0.3, 0.4, 0.41, 0.45, 0.5$, respectively.

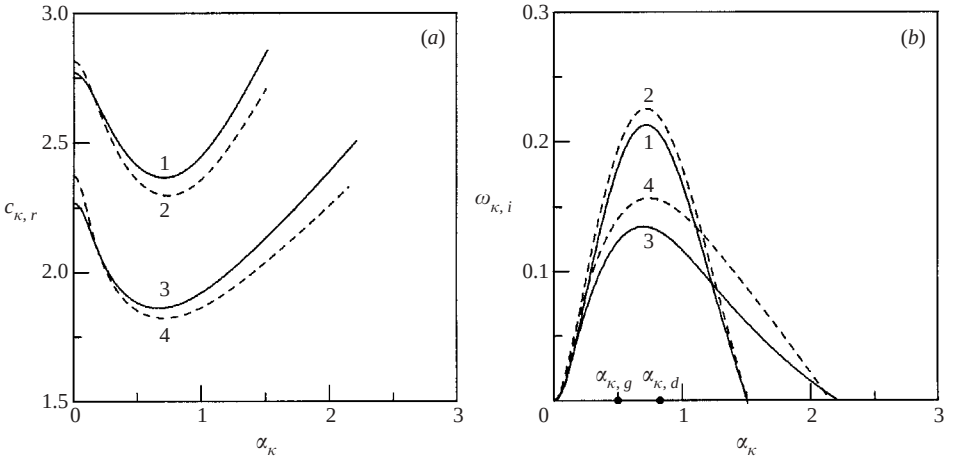

FIGURE 6. (*a*) Velocities $c_{\kappa,r}$ and (*b*) amplification factors $\omega_{\kappa,i}$ of unstable perturbations. Solid curves 1 and 3 are solutions of the eigenvalue problem (4.4) with $\delta = 0.182$, $E^{-1} = 0.133$ (case $n = 6$, table 1*a*) and $\delta = 0.618$, $E^{-1} = 0.260$ (case $n = 2$, table 1*c*), respectively. Dashed curves, 2 and 4, are solutions of the linearized Navier–Stokes equations and boundary conditions for the same parameters and $\gamma = 10800$; details are given in Sisoev & Shkadov (1987, 1990). Wavenumbers $\alpha_{\kappa,g} = 0.5$ and $\alpha_{\kappa,d} = 0.89$ are experimental values, corresponding to the case $n = 6$, table 1(*a*) and the case $n = 2$, table 1(*c*), respectively.

Thus, decreasing the Eckman number has a stabilizing effect according to the linear theory, in agreement with the conclusion of Charwat *et al.* (1972).

To verify the results of the linear stability analysis, carried out using the localized equations (4.2), the eigenvalues were also computed for the full Navier–Stokes problem for flow of a liquid layer over a spinning disk (2.3). The examples presented in figure 6 were computed for the case $\gamma = 10800$ which is typical of experiments. The agreement is very good: these localized equations adequately capture the properties of the full problem. The ranges of unstable wavelengths, phase velocities and amplification

factors determined from the approximate model correspond well with the correct values determined from the full equations.

4.3. *Regular waves*

The nonlinear travelling wave solutions of equations (4.2) are sought in the form

$$h(\eta), \quad q(\eta), \quad p(\eta), \quad \eta = \omega_\kappa(\lambda_\kappa x_\kappa - t_\kappa),$$

with wave velocity $c_\kappa = \lambda_\kappa^{-1}$. Integration of the continuity equation gives

$$q = \frac{h - h_m}{\lambda_\kappa} + 1,$$

where h_m is the average film thickness, and the average flow rate is unity because of the choice of scaling. The nonlinear eigenvalue problem for the periodic functions $h(\eta)$ and $p(\eta)$, the average film thickness h_m and the inverse wave velocity λ_κ is

$$(\lambda_\kappa\omega_\kappa h)^3\frac{\mathrm{d}^3h}{\mathrm{d}\eta^3} - \frac{\omega_\kappa\delta}{\lambda_\kappa}[h^2 - 6(h_m - \lambda_\kappa)^2]\frac{\mathrm{d}h}{\mathrm{d}\eta} - \frac{h - h_m}{\lambda_\kappa} - 1 + h^3 + \frac{2h^2p}{E} - \frac{h}{3E^2}\left[\beta_{12}\left(\frac{h - h_m}{\lambda_\kappa} + 1\right)^2 - 3\beta_{13}p^2\right] = 0, \quad (4.5a)$$

$$\omega_\kappa h[(\beta_{21} - 1)h - \beta_{21}(h_m - \lambda_\kappa)]\frac{\mathrm{d}p}{\mathrm{d}\eta} + \beta_{21}\omega_\kappa(h_m - \lambda_\kappa)p\frac{\mathrm{d}h}{\mathrm{d}\eta} + \frac{1}{15\delta}\left[\beta_{23}p + \frac{2h^2}{E}\left(\frac{h - h_m}{\lambda_\kappa} + 1\right)\right] + \frac{\beta_{22}ph}{15\delta E^2}\left(\frac{h - h_m}{\lambda_\kappa} + 1\right) = 0, \quad (4.5b)$$

$$h(\eta) = h(\eta + 2\pi), \quad \left.\frac{\mathrm{d}h}{\mathrm{d}\eta}\right|_\eta = \left.\frac{\mathrm{d}h}{\mathrm{d}\eta}\right|_{\eta+2\pi}, \quad \left.\frac{\mathrm{d}^2h}{\mathrm{d}\eta^2}\right|_\eta = \left.\frac{\mathrm{d}^2h}{\mathrm{d}\eta^2}\right|_{\eta+2\pi}, \quad (4.5c\text{–}e)$$

$$p(\eta) = p(\eta + 2\pi), \quad \frac{1}{2\pi}\int_\eta^{\eta+2\pi} h\,\mathrm{d}\eta = h_m. \quad (4.5f, g)$$

The problem (4.5) includes two external dimensionless parameters δ and E and the frequency ω_κ which is an internal parameter of the problem.

The two-parameter manifold of solutions of (4.5) in the case $E^{-1} = 0$, which corresponds to steady waves in a falling film, has been investigated over many years (Chang & Demekhin 2002). A very detailed analysis of the solutions was presented by Sisoev & Shkadov (1999), where inherent peculiarities, with co-dimension 1 and 2, were investigated. We use this analysis as a basis to investigate the similarities and differences between the falling film and spinning disk flows. Solutions of the problem (4.5) have been computed numerically by the method of invariant embedding, first applied to the flow in a falling film by Bunov *et al.* (1984).

It is usual to describe the solutions of the problem (4.5) in terms of *families of waves*. Each family is a smooth set of solutions, parameterized by a single quantity ω_κ for fixed values of the external parameters δ and E. Before discussing the case of finite E we briefly describe typical wave solutions at $E^{-1} = 0$, corresponding to the falling film.

In figure 7(*a*) the velocities of waves in several families which are most relevant to the experimental observations are presented. Each family is identified by a notation

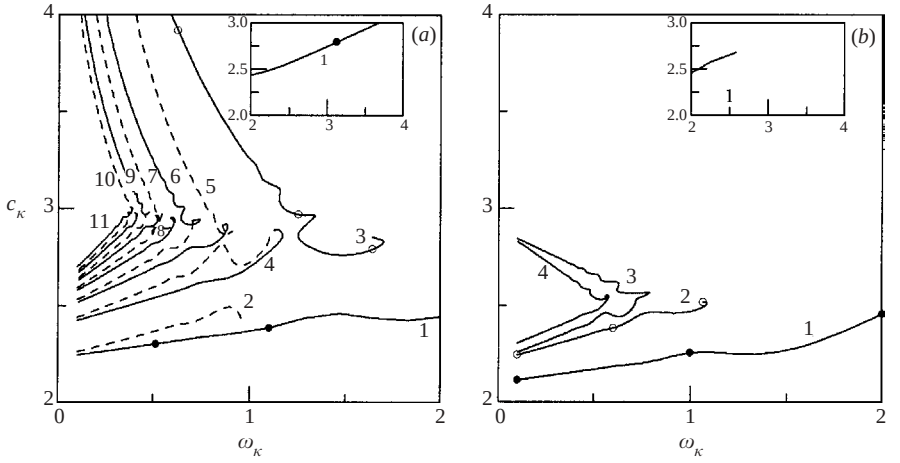

FIGURE 7. Velocities of steady waves at $\delta = 0.1$. (*a*) $E^{-1} = 0$. The labels correspond to the following families: 1, $\gamma_{-1,1}$; 2, $\gamma_{-1,2}$; 3, $\gamma_{+1,1}$; 4, $\gamma_{-2,1}$ and $\gamma_{-2,2}$; 5, $\gamma_{-3,1}$ and $\gamma_{+1,2}$; 6, $\gamma_{-3,2}$ and $\gamma_{+2,1}$; 7, $\gamma_{-4,1}$ and $\gamma_{+2,2}$; 8, $\gamma_{-4,2}$ and $\gamma_{-5,1}$; 9, $\gamma_{-5,2}$ and $\gamma_{+3,1}$; 10, $\gamma_{-6,1}$ and $\gamma_{+3,2}$; 11, $\gamma_{-6,2}$ and $\gamma_{-7,1}$. Solid and dashed curves denote one-humped and two-humped families, respectively. Solid and open circles denote the waves of the first family $\gamma_{-1,1}$ and the second family $\gamma_{+1,1}$ shown in figure 9. (*b*) $E^{-1} = 0.2$. 1, $\gamma_{-1,1}$; 2, $\gamma_{-2,1}$; 3, $\gamma_{-2,2}$ and $\gamma_{+1,1}$; 4, $\gamma_{-3,1}$ and $\gamma_{+1,2}$. Solid and open circles correspond to the waves from the families $\gamma_{-1,1}$ and $\gamma_{-2,1}$ shown in figure 11.

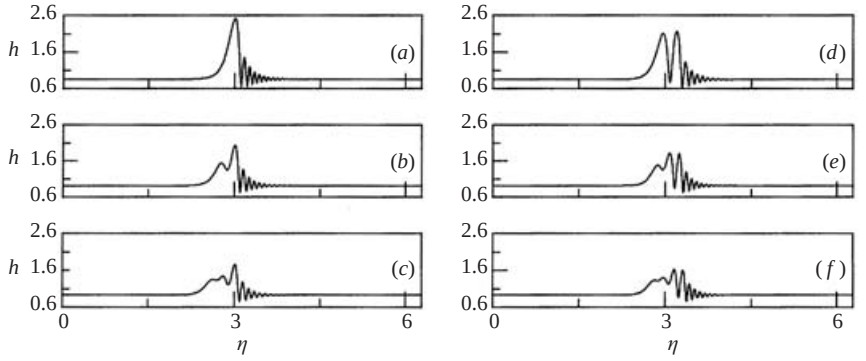

FIGURE 8. Fast one- and two-humped families at $\delta = 0.1$, $E^{-1} = 0$ and $\omega_\kappa = 0.1$: (*a*) $\gamma_{+1,1}$, (*b*) $\gamma_{+2,1}$, (*c*) $\gamma_{+3,1}$, (*d*) $\gamma_{+1,2}$, (*e*) $\gamma_{+2,2}$, (*f*) $\gamma_{+3,2}$.

$\gamma_{\pm m,j}$ that is based on the properties of the solutions. The sign of m refers to the velocity relative to the neutral velocity $c_{\kappa,n} = 3$: negative m corresponds to slow waves ($c_\kappa < 3$ for small ω_κ) and positive m to fast waves ($c_\kappa > 3$ for small ω_κ). For finite values of E, the velocity of neutral waves $c_{\kappa,n}$ is close to 3, but the same notation can be applied without ambiguity (figure 7*b*). Typical shapes of fast waves are shown in figure 8. The value of j corresponds to the number of main humps in a wave shape: one-humped fast waves are shown in figure 8(*a–c*), two-humped fast waves in figures 8(*d–f*). The index m is the index number of the wave in the system of waves belonging to the fast (or slow) one-humped (or two-humped) families; increasing m corresponds to an increase of the velocity for the set of slow families and to a decrease of the velocity for the set of fast families (see figure 7).

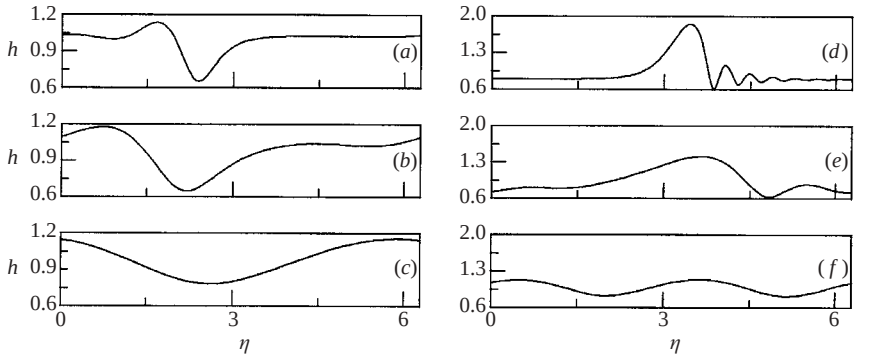

FIGURE 9. $\delta = 0.1$, $E^{-1} = 0$. Waves of the first family $\gamma_{-1,1}$: (*a*) $\omega_\kappa = 0.5$, (*b*) $\omega_\kappa = 1.1$, (*c*) $\omega_\kappa = 3.1$. Waves of the second family $\gamma_{+1,1}$: (*d*) $\omega_\kappa = 0.6$, (*e*) $\omega_\kappa = 1.3$, (*f*) $\omega_\kappa = 1.6$.

Among all of the wave families, the two most important are the first family $\gamma_{-1,1}$ (Shkadov 1967), with the lowest velocity, and the second family $\gamma_{+1,1}$ (Bunov *et al.* 1984), with the greatest velocity in the interval of wavenumbers where it exists, shown in figure 9 at different frequencies; the wave of the second family is also shown in figure 8(*a*) for $\omega_\kappa = 0.1$. Each family has a bifurcation point (the ends of the lines in figure 7*a*) beyond which waves of that family cease to exist. The waves of the first family near the bifurcation point (which lies on the neutral curve) have a sinusoidal shape with one harmonic, as illustrated in figure 9(*c*). There are two harmonics near the bifurcation point of the second family at small values of δ (figure 9*f*) but this increases with increasing δ.

All the wave families shown in figure 7(*a*), except $\gamma_{-1,1}$, $\gamma_{-1,2}$ and $\gamma_{+1,1}$, have a joint bifurcation point with another family, belonging to the alternative one-humped or two-humped class. To underline this, one-humped families are shown as solid curves and two-humped families as dashed curves. For values of $\delta = 0.1$ or smaller, it is not possible to pass through the bifurcation point using the numerical method applied here, due to the lack of smoothness of the solution families.

As well as expanding the interval of unstable frequencies, as shown in figure 5, increasing δ leads to significant changes in the diagram of wave families. Comparing figures 7(*a*) and 10(*a*) we see that the bifurcation point of the second family moves to a lower frequency; other fast-wave families have bifurcation points to left of this one. The region of relatively high-frequency waves is filled in by the slow-wave families, some of whose bifurcation points are smooth enough to traverse numerically. In addition, at $\delta = 0.3$, it is the slow one-humped family $\gamma_{-2,1}$ that has an unshared bifurcation point, rather than the second family $\gamma_{+1,1}$ at $\delta = 0.1$. Further increase of δ leads to the disappearance of the fast families at any fixed frequency ω_κ.

In what follows, we will exploit the families which contain waves with the greatest velocity for some range of ω_κ, at given values of δ and E. The greatest wave velocity is associated with the highest (peak) film thickness. We shall use the terminology *dominating waves* (Sisoev & Shkadov 1997*a*, *b*) to describe these waves without explicitly verifying their attracting properties.

The effect of finite values of the Eckman number on the families which contain waves with the greatest velocity can be seen in figures 7(*b*) and 10(*b*) where the case $E^{-1} = 0.2$ is presented for $\delta = 0.1$ and 0.3, respectively. In the case $\delta = 0.1$ we see a very strong effect of the Eckman number. First, in accordance with figure 5, the interval of unstable frequencies becomes narrower. Secondly, there is a displacement

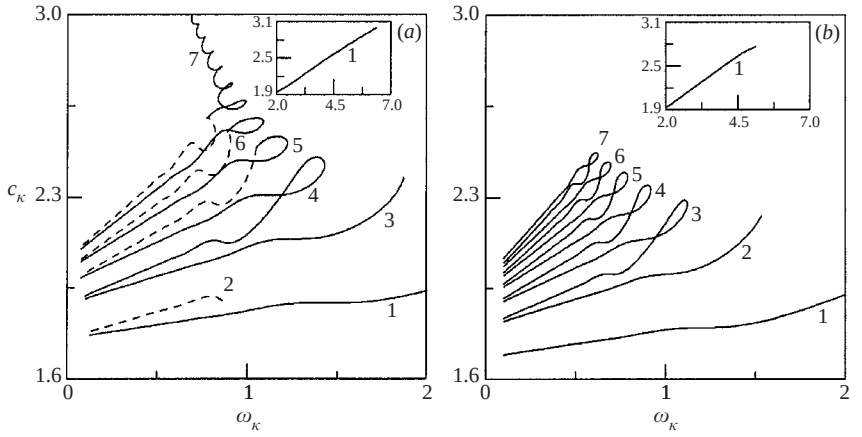

FIGURE 10. Velocities of steady waves at $\delta = 0.3$. (*a*) $E^{-1} = 0$. The labels correspond to the following families: 1, $\gamma_{-1,1}$; 2, $\gamma_{-1,2}$; 3, $\gamma_{-2,1}$; 4, $\gamma_{-2,2}$ and $\gamma_{-3,1}$; 5, $\gamma_{-3,2}$ and $\gamma_{-4,1}$; 6, $\gamma_{-4,2}$ and $\gamma_{-5,1}$; 7, $\gamma_{-5,2}$ and $\gamma_{+1,1}$. (*b*) $E^{-1} = 0.2$. 1, $\gamma_{-1,1}$; 2, $\gamma_{-2,1}$; 3, $\gamma_{-2,2}$ and $\gamma_{-3,1}$; 4, $\gamma_{-3,2}$ and $\gamma_{-4,1}$; 5, $\gamma_{-4,2}$ and $\gamma_{-5,1}$; 6, $\gamma_{-5,2}$ and $\gamma_{-6,1}$; 7, $\gamma_{-6,2}$ and $\gamma_{-7,1}$.

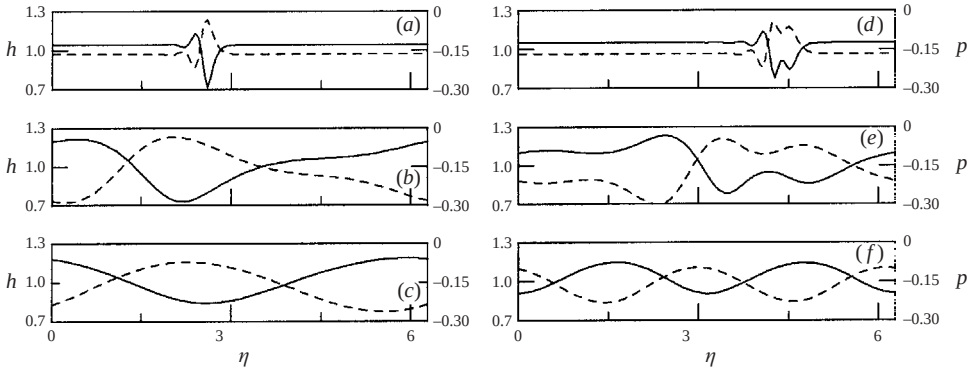

FIGURE 11. Film thickness h (solid curve) and azimuthal flow rate p (dashed curve) at $\delta = 0.1$, $E^{-1} = 0.2$. Waves of the first family $\gamma_{-1,1}$: (*a*) $\omega_\kappa = 0.1$, (*b*) $\omega_\kappa = 1$, (*c*) $\omega_\kappa = 2$. Waves of the family $\gamma_{-2,1}$: (*d*) $\omega_\kappa = 0.1$, (*e*) $\omega_\kappa = 0.6$, (*f*) $\omega_\kappa = 1.065$.

of the bifurcation points of the fast families towards the low-frequency range, which is similar to the effect of increasing δ. To illustrate typical wave shapes, we consider waves belonging to the slow one-humped families with largest bifurcation frequencies. The shapes of the slow one-humped families presented in figure 11 are very similar to the falling film case shown in figure 9(*a–c*): the Eckman number effect is quantitative but not qualitative. The plots of the azimuthal flow rate, included in figure 11, demonstrate that this function is out of phase with the film thickness along a wave: the difference in azimuthal velocity at the disk surface and at the interface increases with increasing film thickness.

The effect of increasing E^{-1} at $\delta = 0.3$ is demonstrated in figure 10. The bifurcation points of the slow one-humped and two-humped families denoted as curves 1, 3–6 at $E^{-1} = 0$ are shifted to lower frequencies at $E^{-1} = 0.2$ (curves 1–5). The fast one-humped family $\gamma_{+1,1}$, which bifurcates with the slow two-humped family $\gamma_{-5,2}$ at $E^{-1} = 0$ (curve 7 in figure 10*a*) is replaced by the slow one-humped family $\gamma_{-6,1}$ at

$E^{-1} = 0.2$ (curve 6 in figure 10*b*). Hence, the principal effect of increasing E^{-1} from 0 to 0.2 for this larger value of δ is a shift of the bifurcation points towards the low-frequency region.

The results presented in this section have elucidated the structure of the families of regular wave solutions of the localized equations (4.2). Recall that the problem we have solved, (4.5), corresponds to a truncated version of the evolution system (2.9). Two issues are important in comparing with experimental results: parametric continuation of the solutions of the falling film problem to finite Eckman number and the effect this has on the computed solutions. In the next section, we apply the solutions of (4.5) to explain previously published experimental results.

5. Comparison with the experiments of Woods (1995)

As was mentioned in the Introduction, we know of only one experimental investigation (Woods 1995) that reports sufficient details about finite-amplitude wave regimes on a spinning disk. In these experiments, a camera was placed below the disk and connected to a computer which provided video imaging hardware and software. The recorded image area was $15 \times 12\,\mathrm{mm}^2$, which is greater than the sizes of the observed waves. Preliminary investigations were carried out to tune the system for precise measurement of the film thickness in the wavy flow regimes. The liquid used, water with nigrosene dye, had the following properties: viscosity $\nu = 0.01\,\mathrm{cm}^2\,\mathrm{s}^{-1}$ and surface tension $\sigma = 49.5$ dyn cm^{-1}. The author did not report the liquid density, so we use the value $\rho = 1\,\mathrm{g\,cm}^{-3}$. In the experiments, the dimensional parameters were: flow rate $Q_c = 7, 13, 19\,\mathrm{cm}^3\,\mathrm{s}^{-1}$ and rotational velocity $\Omega = 100, 200, \ldots, 600$ r.p.m. Measurements of maximum film thickness were presented at four points along the radius $\tilde{r} = 5.45, 8.1, 11.3, 14.4$ cm. Some of the cases presented in Woods (1995) are summarized in tables 1(*a*), 1(*b*) and 1(*c*), where values of the dimensionless parameters introduced above are also given. Short descriptions of the visually observed wave regimes are also given: 2D and 3D correspond to two-dimensional or axisymmetric waves, and three-dimensional wave structures, respectively. In the cases where the observed axisymmetric waves are close to the local periodic wave solutions, we have calculated the dimensionless wavenumber $\alpha'_\kappa = \omega'_\kappa \lambda'_\kappa$ for comparison with the solutions of the nonlinear eigenvalue problem (4.5).

The table shows that the value of ε^2/κ^2 is always small, so that the assumptions used in the derivation of the system (2.9) are fulfilled; we have checked that this is indeed the case for all the experiments of Woods (1995). This means that the basic hypothesis of modelling finite-amplitude capillary waves in terms of a balance of inertial, viscous and capillary forces is confirmed for film flow on a spinning disk in the same manner as it was for the falling film when it was first considered by Shkadov (1967). The value of κ is also small, which allows us to use the localized equations (4.2).

Comparison of the parameters of the measured local 2D wave structures with the solutions of (4.5) is based on the assumption that the properties of the problem (2.9) are qualitatively similar to those of the falling film system and that the local dominating waves will be realized despite the radial variation of the parameters δ' and E'. For each experimental measurement of Woods (1995), corresponding to a unique pair of the governing parameters δ' and E', we will try to find a solution for comparison among the families with dominating waves.

The procedure used is as follows. Among the instantaneous 2D wave profiles given by Woods (1995), we select those that are close to spatially periodic; the length and

	n	Ω, r.p.m.	R_c, cm	$\tilde{h}_{max}$, mm	κ $\times 10$	ε^2/κ^2 $\times 10$	δ'	$(E')^{-1}$	$\tilde{h}_{max}/\tilde{h}_N$, exp.	α'_κ, exp.	Wave regimes
(a)	1	100	5.45	0.28	0.198	0.196	0.243	0.285	1.294		smooth
	2	100	8.10	0.18	0.107	0.180	0.156	0.168	1.087		smooth
	3	100	11.30	0.14	0.064	0.167	0.108	0.108	1.081		2D
	4	**100**	**14.40**	**0.15**	**0.044**	**0.158**	**0.082**	**0.078**	**1.295**	**0.52**	**2D**
	5	**200**	**5.45**	**0.18**	**0.107**	**0.267**	**0.283**	**0.226**	**1.305**	**1.11**	**2D**
	6	**200**	**8.10**	**0.17**	**0.058**	**0.244**	**0.182**	**0.133**	**1.650**	**0.50**	**2D**
	7	200	11.30	0.15	0.034	0.227	0.126	0.086	1.810		2D
	8	200	14.40	0.11	0.024	0.215	0.096	0.062	1.541		3D
	9	**300**	**5.45**	**0.15**	**0.074**	**0.320**	**0.310**	**0.198**	**1.434**	**0.57**	**2D**
	10	300	8.10	0.14	0.040	0.293	0.199	0.117	1.801		3D
(b)	**1**	**200**	**5.45**	**0.22**	**0.114**	**0.352**	**0.603**	**0.342**	**1.328**	**0.88**	**2D**
	2	200	8.10	0.23	0.062	0.322	0.388	0.202	1.749		2D
	3	200	11.30	0.23	0.037	0.299	0.268	0.129	2.184		3D
	4	200	14.40	0.18	0.025	0.283	0.205	0.094	2.000		3D
(c)	1	200	5.45	0.29	0.119	0.416	0.959	0.440	1.541		2D
	2	**200**	**8.10**	**0.23**	**0.064**	**0.381**	**0.618**	**0.260**	**1.541**	**0.83**	**2D**
	3	200	11.30	0.25	0.038	0.354	0.427	0.167	2.148		3D
	4	200	14.40	0.25	0.026	0.335	0.326	0.121	2.473		3D
	5	**300**	**5.45**	**0.21**	**0.083**	**0.498**	**1.050**	**0.385**	**1.443**	**0.68**	**2D**
	6	300	8.10	0.22	0.045	0.456	0.676	0.227	1.973		2D
	7	300	11.30	0.29	0.027	0.424	0.467	0.145	3.284		3D
	8	300	14.40	0.25	0.018	0.402	0.357	0.105	3.274		3D
	9	**400**	**5.45**	**0.19**	**0.064**	**0.566**	**1.119**	**0.349**	**1.573**	**0.38**	**2D**
	10	400	8.10	0.26	0.035	0.519	0.721	0.206	2.788		2D

TABLE 1. Selected experiments at (a) $Q_c = 7$ cm^3 s^{-1}, (b) 13 cm^3 s^{-1} and (c) 19 cm^3 s^{-1} (Woods, 1995). 2D wave regimes are shown bold for clarity.

maximum height of the wave, taken from separate plots presented by Woods (1995), are scaled into the plane $(\alpha'_\kappa, h'_{max})$. The families of quasi-steady waves, to which the dominating waves belong, are then computed at the relevant values of δ' and E' and shown on the same plot. If the experimental point is on or near any theoretical curve, we can compare the corresponding solution of (4.5) with the shape of the wave observed in the experiment.

The first examples are presented in figures 12(a, b) and 13(a, b), where waves of the basic families, the first family (figure 13b) and the second family (figure 13a), are shown. It is important to note that waves of the first family are not observed experimentally at such large values of δ' for falling films (in the absence of forcing at the inlet). This, however, is not the case for flow over a spinning disk, due to the stabilizing effect of the Coriolis force at finite Eckman number. The computed and experimental wave profiles are in good quantitative agreement.

It is known that, for the falling film, subcritical oscillations in the vicinity of the first family waves may lead to waves of larger amplitude. Examples are given in figures 12(c, d) and 13(c, d); these cases correspond to similar values of the governing parameter δ'. The case of $n = 2$, table 1(c), however, is more 'unstable' because the δ' value is slightly larger and $(E')^{-1}$ is smaller. This is reflected in the significantly larger wave amplitude observed in figures 12(d), 13(d), than in figures 12(c), 13(c). These cases are particularly interesting because the dimensionless frequencies of the waves calculated from the experimental conditions are similar ($\omega'_\kappa = 1.34$ for 13c and

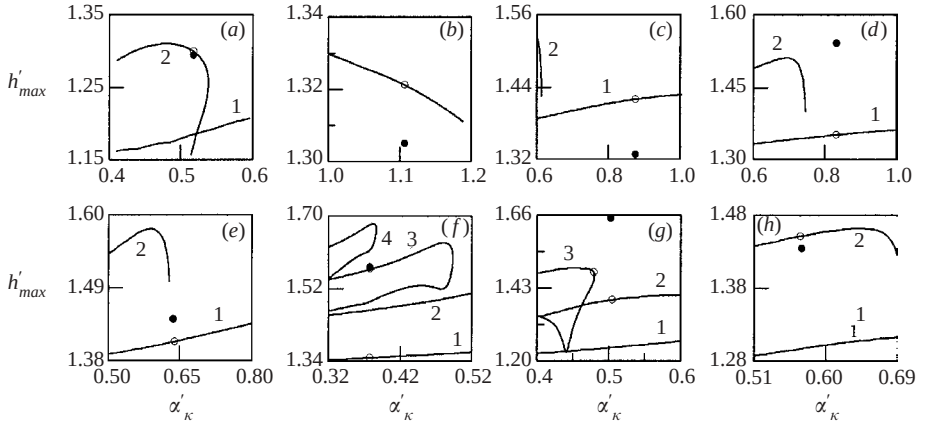

FIGURE 12. Comparison of wave parameters measured by Woods (1995) (solid circles) with computed families; open circles correspond to the waves presented in figure 13. (*a*) $\gamma_{-1,1}$ (curve 1) and $\gamma_{+1,1}$ (curve 2) for $n = 4$, table 1(*a*). (*b*) $\gamma_{-1,1}$ for $n = 5$, table 1(*a*). (*c*) $\gamma_{-1,1}$ (curve 1) and $\gamma_{+1,1}$ (curve 2) for $n = 1$, table 1(*b*). (*d*) $\gamma_{-1,1}$ (curve 1) and $\gamma_{+1,1}$ (curve 2) for $n = 2$, table 1(*c*). (*e*) $\gamma_{-1,1}$ (curve 1) and $\gamma_{-2,1}$ (curve 2) for $n = 5$, table 1(*c*). (*f*) $\gamma_{-1,1}$ (curve 1), $\gamma_{-2,1}$ (curve 2), $\gamma_{-3,1}$–$\gamma_{-2,2}$ (curve 3) and $\gamma_{-4,1}$–$\gamma_{-3,2}$ (curve 4) for $n = 9$, table 1(*c*). (*g*) $\gamma_{-1,1}$ (curve 1), $\gamma_{-2,1}$ (curve 2) and $\gamma_{-3,1}$–$\gamma_{-2,2}$ (curve 3) for $n = 6$, table 1(*a*). (*h*) $\gamma_{-1,1}$ (curve 1) and $\gamma_{-2,1}$ for $n = 9$, table 1(*a*).

$\omega'_\kappa = 1.28$ for 13(*d*), so it is possible to compare the behaviour of the waves at different values of the governing parameters. Furthermore, it may be seen in figure 6(*b*) that the wavelength observed in figure 13(*d*), $\alpha'_{\kappa,d}$, is very close to that of the fastest growing linear mode.

Developing waves in the vicinity of bifurcation points are presented in figures 12(*e*, *f*) and 13(*e*, *f*). These measurements were made at the smallest value of the radius and are in the initial stage of wave formation. In figure 13(*e*) a possible quasi-steady wave of the first family is presented, while figure 13(*f*) shows two candidate solutions. In both cases, the observed wave has a shape similar to the dominating wave of the first family, but with a different amplitude. This situation is also typical of developing waves in a falling film in the initial stage of nonlinear evolution. It is important to note that naturally developing waves very often have frequencies (or wavelengths) close to the bifurcation points of so-called intermediate families (Shkadov & Sisoev 2000). This situation was observed experimentally for falling films (Alekseenko *et al.* 1992). The example presented in figure 12(*f*) demonstrates the role of the intermediate wave regimes in the case of film flow over a spinning disk.

In figures 12(*g*, *h*) and 13(*g*, *h*) the measured waves have similar frequencies: $\omega'_\kappa = 1.18$ in figure 13(*g*) and $\omega'_\kappa = 1.14$ in figure 13(*h*). The measured wave shapes are also very similar. But due to the sensitivity of the structure of the families to variation of the governing parameters, the waves shown represent a subcritical oscillation regime (Shkadov & Sisoev 2000) in figure 13(*g*) and a limiting dominating wave in figure 13(*h*). It is interesting that the latter case corresponds to a smaller radial position. It is also noteworthy that the wavelength in the case shown in figure 13(*g*), $\alpha'_{\kappa,g}$, is close to that of the fastest growing linear disturbance, as shown in figure 6.

This detailed comparison of theoretical results with experimental measurements leads to two important conclusions. Firstly, the conditions of the experiments, in

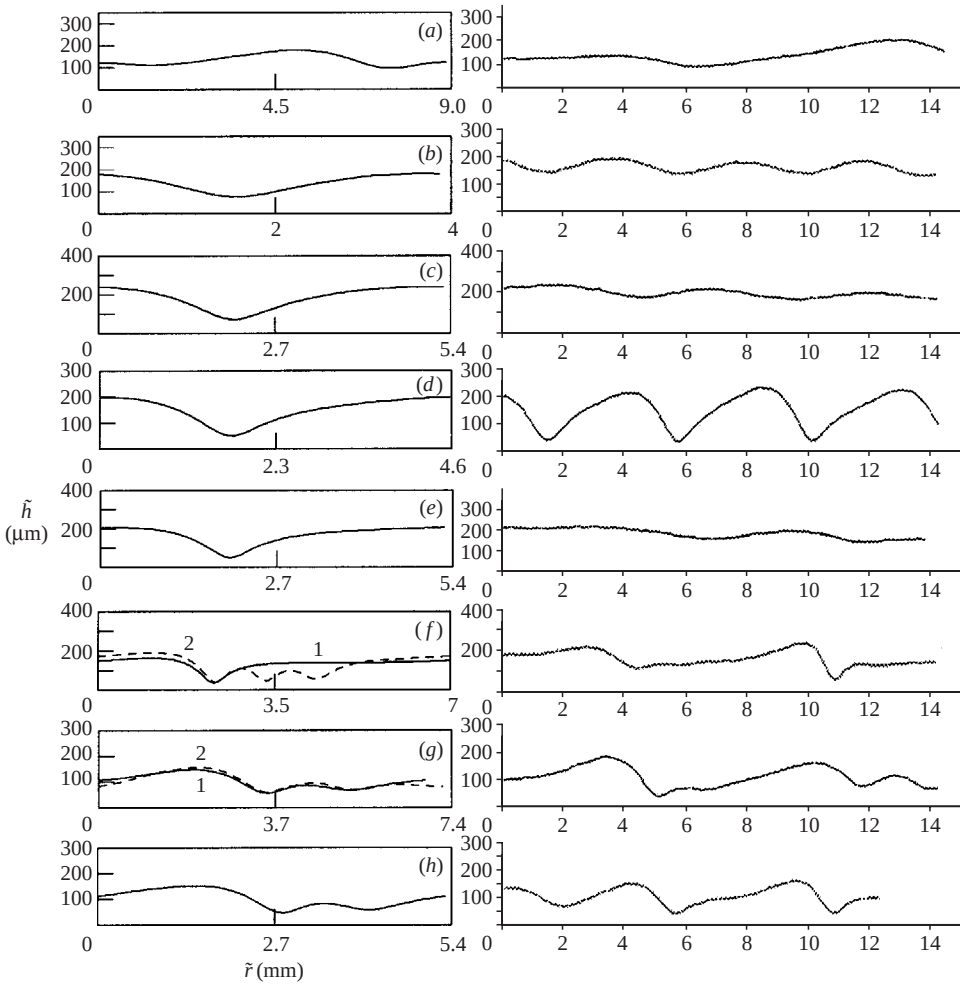

FIGURE 13. Measured waves (right) and computed waves (left): (*a*) $\gamma_{+1,1}$ for $n = 4$, table 1(*a*), (*b*) $\gamma_{-1,1}$ for $n = 5$, table 1(*a*), (*c*) $\gamma_{-1,1}$ for $n = 1$, table 1(*b*), (*d*) $\gamma_{-1,1}$ for $n = 2$, table 1(*c*), (*e*) $\gamma_{-1,1}$ for $n = 5$, table 1(*c*), (*f*) $\gamma_{-3,1}$ (curve 1), $\gamma_{-2,2}$ (curve 2) for $n = 9$, table 1(*c*), (*g*) $\gamma_{-2,1}$ (curve 1), $\gamma_{-3,1}$–$\gamma_{-2,2}$ (curve 2) for $n = 6$, table 1(*a*) (*h*) $\gamma_{-2,1}$ for $n = 9$, table 1(*a*).

which quasi-periodic wave regimes were observed, satisfy the assumptions used to derive the system of model equations (2.9). Secondly, some of the measured wave structures correspond closely to travelling-wave solutions of the localized system (4.2) both qualitatively and quantitatively. Typical cases have been observed: a wave of the first family (figure 12*b*), a wave of the second family (figure 12*a*), a wave of an intermediate family (figure 12*h*), an oscillating subcritical wave regime (figure 12*d*), and a developing wave regime (figure 12*f*).

There are a few data, at the smallest rotational speed, with $\tilde{h}_{max} < \tilde{h}_N$ in Woods (1995). According to the images shown, these experiments did not produce any visible waves at the radial positions where measurements were made; the wave structures occur at larger radial distances. These results therefore correspond to the inlet region wherein waves had not yet formed; in fact, the steady waveless solution of (3.1) is expected in the inlet region (see figures 1 and 2).

6. Discussion

The model (2.9) derived above is intended to describe real finite-amplitude waves in flow over a spinning disk. There are two important issues in the comparison of theoretical and experimental results. The first is related to whether the radius of the disk used in the experiments is sufficiently large for regular waves to form. Investigations of falling films have demonstrated that very long plates may be required to observe regular waves or deterministic oscillating regimes, as demonstrated by Alekseenko *et al.* (1992) and Liu & Gollub (1994); in the latter case, an inclined substrate with a length of 200 cm was used.

The second issue is that experiments on spinning disks have been carried out for the case of naturally developing waves only. From the first experimental work of Kapitza & Kapitza (1949) it has been known that the wave regimes in this case are only weakly predictable: experiments with very similar conditions can lead to different wave regimes. In contrast, forcing of harmonic perturbations at the flow inlet allows control of the flow regimes. This has been demonstrated many times (see Liu & Gollub 1994, for example). It is important to note that perturbations may be initiated by the spinning disk itself, but in the experiments of Woods (1995), the dimensionless rotational frequency is very small, $\omega'_{\kappa} \in (0.02; 0.13)$, and the observed wave frequencies were significantly greater than the disk frequencies. This experimental observation is in accordance with known results for the falling film: it was noted by Kapitza & Kapitza (1949) that as the frequency of forcing is reduced, regular waves are generated with longer wavelengths, but only up to some critical value, beyond which regular waves cannot be generated. To elucidate this critical wavelength, computations of wave evolution into a large spatial domain were carried out by Chang, Demekhin & Kalaidin (1995, 1996*a*, *b*). Analysis of the stability of nonlinear regular waves by Shkadov & Sisoev (2001) has shown that the critical wavelength (or corresponding frequency) is related to bifurcations of the second family. There is a jump transition of the limiting wave regime from the second family to families bifurcating from it; the new limiting waves have length (or frequency) 2, 3, ... times greater than that generated at the flow inlet. On the physical level, the falling film is not sensitive to very slow periodic perturbations; the film flow over a spinning disk demonstrates a similar insensitivity to forcing at the rotational frequency. Analysis of the stability of nonlinear periodic waves is, however, beyond the scope of the present work.

In addition, the present work is restricted to the class of local periodic wave solutions that allows us to apply effective numerical procedures; here we have used fast Fourier transforms. Referring again to the falling film, it is known that limiting periodic waves may not be achieved in many cases, due to multiple bifurcations of the wave families. This problem might have been expected in the present study of flow over a spinning disk because formation of the limiting steady wave or oscillating regime might require a large propagation distance that might greatly exceed the radius of the disk used in the experiments. Nevertheless, based on experimental observations in which local nearly periodic waves were observed, we have sought such waves as solutions of the localized equations (4.2). In each case where we found experimental waves close to a periodic solution, either the experimentally observed wave coincides with a dominating wave, both in parameters and shape, or its parameters correspond to an oscillating regime in the vicinity of a bifurcation point. In general, the correspondence between the theoretical computations and the measured waves is better than could have been expected, despite the variation of the body force in the radial direction.

n	Ω, r.p.m.	R_c, cm	Q_c, cm^3 s^{-1}	$\nu \times 10$, cm^2 s^{-1}	ρ, g cm^{-3}	κ $\times 10^2$	ε^2/κ^2 $\times 10$	δ'	$(E')^{-1}$
1	2291	6.5	5.50	0.10	1.0	0.099	0.568	0.273	0.068
2	1909	6.0	9.50	0.10	1.0	0.140	0.679	0.559	0.115
3	1795	6.5	6.50	0.10	1.0	0.125	0.548	0.317	0.082
4	998	16.0	6.50	0.10	1.0	0.052	0.346	0.102	0.030
5	2291	7.5	22.73	0.47	1.1	0.107	2.190	0.409	0.086
6	1718	9.0	22.73	0.47	1.1	0.104	1.850	0.313	0.074
7	1336	11.0	30.00	0.47	1.1	0.098	1.790	0.333	0.074

TABLE 2. Experimental parameters of Butuzov & Puhovoi (1976).

The results of other experimental investigations are less straightforward to analyse, since the data reported are less complete than those of Woods (1995). Calculations from of experimental results of Matsumoto *et al.* (1973) show that the assumption $\varepsilon^2/\kappa^2 \ll 1$ is satisfied in most cases, and is borderline in others. However, no information is given about wave structures by Matsumoto *et al.* (1973), which distinguishes this paper from other studies. Furthermore, the maximum film thickness is very close to the Nusselt value. The explanation lies in the values of the similarity parameters in this investigation. The experimental runs may be provisionally divided into two groups. The first consists of experiments conducted at very small values of $\delta'(\leqslant 0.04)$ when, even without the stabilizing effect of the Coriolis forces, wave regimes cannot be measured due to the very small wave amplitudes. Other measurements, at larger δ' values, also have finite Eckman number values. The largest value, $\delta' = 0.77$, occurs at $(E')^{-1} = 0.374$, which indicates a strongly stabilizing Coriolis effect. There are additional circumstances that could contribute to the lack of wave observations. For instance, because the radial distances at which measurements were made were small, the wave formation may not have been sufficiently advanced; a few runs with $\tilde{h}_{max} < \tilde{h}_N$ support this conjecture.

As mentioned in the Introduction, the critical radius dividing the domains of axisymmetric waves, in a region nearer the flow origin, and three-dimensional ripples, nearer the disk periphery, was studied by Butuzov & Puhovoi (1976). Calculated values of the similarity parameters at the critical radius are given in table 2, which reveals that the assumptions required for the model (2.9) are fulfilled. In contrast to the work of Matsumoto *et al.* (1973), the flow regimes studied by Butuzov & Puhovoi (1976) near the critical radius correspond to finite values of δ', which are similar to those observed in experiments on falling films, and large Eckman numbers. Moreover, the calculated values of the wave parameters in the upstream region confirm that the flows of Butuzov & Puhovoi (1976) may be modelled by (2.9). Unfortunately, their paper does not include any quantitative data on wave shapes or parameters.

The results of experiments by Rifert *et al.* (1982) are presented in table 3; water was used and measurements were made at $R_c = 9$ cm where a wave regime had developed. As in the experimental studies described previously, the conditions under which wave regimes were realized are consistent with the assumptions of the model (2.9). It may be noted that the maximum film thickness is less than the Nusselt thickness in two cases, runs 5 and 12, but these measurements were for very thin films and consequently have decreased accuracy. It was noted by Rifert *et al.* (1982) that the majority of experimental points for $Q_c/(2\pi R_c \nu) \leqslant 30$ (runs 1–9) are in good agreement with an approximate result presented by Kholpanov, Shkadov & Malusov 1971) for the

n	Ω, r.p.m.	Q_c, cm^3 s^{-1}	$\tilde{h}_{max}$, mm	κ $\times 10$	ε^2/κ^2 $\times 10$	δ'	$(E')^{-1}$	$\tilde{h}_{max}/\tilde{h}_N$, exp.
1	79	6.8	0.246	0.125	0.122	0.113	0.155	1.371
2	278	6.8	0.162	0.041	0.212	0.149	0.102	2.090
3	596	6.8	0.069	0.021	0.298	0.176	0.079	1.470
4	1233	6.8	0.029	0.011	0.411	0.207	0.062	1.012
5	1889	6.8	0.021	0.008	0.497	0.228	0.054	0.960
6	278	11.3	0.190	0.044	0.266	0.278	0.143	2.056
7	596	11.3	0.096	0.022	0.374	0.329	0.111	1.728
8	1233	11.3	0.042	0.011	0.516	0.387	0.087	1.219
9	1889	11.3	0.031	0.008	0.624	0.425	0.076	1.215
10	596	19.8	0.133	0.024	0.479	0.652	0.161	1.995
11	1253	19.8	0.050	0.012	0.666	0.769	0.126	1.227
12	1909	19.8	0.029	0.008	0.804	0.844	0.109	0.948

TABLE 3. Experiments Rifert *et al.* (1982).

optimal regimes of the first family for the falling film problem; these regimes have the minimum average film thickness for a given flow rate. This agreement may be attributed to the fact that these observations were made at small values of E^{-1}.

Overall, the comparison of theoretical results and experimental measurements has demonstrated both qualitative and quantitative agreement. All of the assumptions about the flow parameters used to derive the evolution model (2.9) are fulfilled in experiments where waves have been observed. The correspondence between theory and experiments is better than could be expected in view of three significant factors that could reduce such an agreement. The first is the finite size of the disk, which might not allow the waves to develop completely. The second is the complicated appearance of competing waves, and hence the predominance of irregular wave structures. Thirdly, in this paper we have used a truncated form of the system (2.9) to estimate its properties. Certainly, for a rigorous analysis, it would be necessary to solve the system (2.9) itself, which would require boundary conditions at both the inlet and outlet boundaries. For the latter, soft boundary conditions that eliminate upstream growing perturbations have been used for the case of the falling film by Chang *et al.* (1995, 1996*a*, *b*). A similar procedure may be applied for the disk, but in contrast to the falling film, numerical experiments modelling film flow over a spinning disk should be carried out for a bounded domain.

7. Conclusions

A system of nonlinear evolution equations has been formulated to model axisymmetric finite-amplitude capillary waves in film flow over a spinning disk for real experimental conditions. The system involves inertial, viscous, capillary, centrifugal and Coriolis forces and is intended to describe flow regimes observed in experiments at moderate flow rates. The assumptions made in deriving the system are supported by calculation of the corresponding parameters for known experimental investigations. The system contains two dimensionless parameters: the film parameter δ that appears in the theory of falling films and the Eckman number which characterizes the Coriolis forces. Approximate solutions in the form of regular waves (periodic waves travelling with constant velocity) have been investigated. The three-dimensional manifold of these solutions is parameterized by an additional internal parameter such as the

frequency or wavenumber. Detailed comparison of the computed solutions with measured wave shapes has demonstrated qualitative and quantitative agreement.

The numerical results demonstrate the strong stabilizing influence of the Coriolis forces on the wave regimes in comparison with flow in a falling film. The model presented allows prediction and, potentially, control of flow regimes in film flow over a spinning disk.

The present work is a basis for further investigations of non-axisymmetric flow regimes and studies of heat and mass transfer processes in films flowing over a spinning disk.

The authors are grateful to Professor V. Ya. Shkadov of Lomonosov Moscow State University and Professor C. Ramshaw and Dr J. R. Burns of the University of Newcastle upon Tyne for fruitful discussions. This work was supported by the Engineering and Physical Sciences Research Council (UK), project numbers GR/R04676/01 and GR/N34895/01.

REFERENCES

Alekseenko, S. V., Nakoryakov, V. E. & Pokusaev, B. T. 1992 *Wave Flow of Films*. Novosibirsk: Nauka.

Aoune, A. & Ramshaw, C. 1999 Process intensification: heat and mass transfer characteristics of liquid films on rotating discs. *Intl. J. Heat Mass Transfer* **42**, 2543–2556.

Bunov, A. V., Demekhin, E. A. & Shkadov, V. Ya. 1984 On the nonuniqueness of nonlinear wave solutions in a viscous layer. *J. Appl. Math. Mech.* **48** (4), 691–696.

Butuzov, A. I. & Puhovoi, I. I. 1976 On regimes of liquid film flows over a rotating surface. *J. Engng Phys.* **31** (2), 217–224.

Chang, H.-C. & Demekhin, E. A. 2002 *Complex Wave Dynamics in Thin Films*. Elsevier.

Chang, H.-C., Demekhin, E. A. & Kalaidin, E. 1995 Interaction dynamics of solitary waves on a falling film. *J. Fluid Mech.* **294**, 123–154.

Chang, H.-C., Demekhin, E. A. & Kalaidin, E. 1996*a* Scalings of spatio-temporal dynamics in a falling film. *Physica Scripta* T **67**, 67–72.

Chang, H.-C., Demekhin, E. A. & Kalaidin, E. 1996*b* Simulation of noise-driven wave dynamics on a falling film. *AIChE J.* **42**, 1553–1568.

Charwat, A. F., Kelly, R. E. & Gazley, C. 1972 The flow and stability of thin liquid films on a rotating disk. *J. Fluid Mech.* **53**, 227–255.

Demekhin, E. A. & Shkadov, V. Ya. 1984 On three-dimensional nonstationary waves on a downflowing liquid film. *Fluid Dyn.* **19** (5), 21–27.

Dorfman, L. A. 1967 Flow and heat transfer in a viscous liquid layer on a spinning disc. *J. Engng Phys.* **12** (3), 309–316.

Eliseev, V. I. 1983 Spatial stability of film flow on a rotating disk. *J. Appl. Mech. Tech. Phys.* **24** (6), 112–117.

Emslie, A. G., Bonner, F. T. & Peck, L. G. 1958 Flow of a viscous liquid on a rotating disk. *J. Appl. Phys.* **29**, 858–862.

Espig, H. & Hoyle, R. 1965 Waves in a thin liquid layer on a rotating disk. *J. Fluid Mech.* **22**, 671–677.

Kapitza, P. L. 1948 Wave flow of thin viscous films. I. Free flow. *J. Exp. Theor. Phys.* **18**, 2–18.

Kapitza, P. L. & Kapitza, S. P. 1949 Wave flow of thin viscous liquid films. III. Experimental study of wave regime of a flow. *J. Expl. Theore. Phys.* **19** (2), 105–120.

Kholpanov, L. P., Shkadov, V. Ya. & Malusov, V. A. 1971 On calculation of wave characterisics of falling liquid film. *Theore. Found. Chem. Technol.* **5** (4), 559–563.

Leneweit, G., Roesner, K. G. & Koehler, R. 1999 Surface instabilities of thin liquid film flow on a rotating disk. *Exps. Fluids* **26**, 75–85.

Lepekhin, G. I., Ryabchuk, G. V., Tyabin, N. V. & Shulman, E. R. 1981 Viscous liquid flow on a surface of a spinning plane disc. *Theore. Found. Chem. Technol.* **15** (3), 391–397.

Liu, J. & Gollub, J. P. 1994 Solitary wave dynamics of film flows. *Phys. Fluids* **6**, 1702–1712.

Matsumoto, S., Saito, K. & Takashima, Y. 1973 The thickness of a viscous liquid film on a rotating disk. *J. Chem. Engng Japan* **6** (6), 503–506.

Miyasaka, Y. 1974*a* On the flow of a viscous free boundary jet on a rotating disk (1st Report. Theoretical analysis). *Bull. JSME* **17** (113), 1461–1468.

Miyasaka, Y. 1974*b* On the flow of a viscous free boundary jet on a rotating disk (2nd Report. Comparison of experimental results with calculated values by means of film thickness). *Bull. JSME* **17** (113), 1469–1475.

Myers, T. G. 1998 Thin films with high surface tension. *SIAM Rev.* **40**, 441–462.

Myers, T. G. & Charpin, J. P. F. 2001 The effect of the Coriolis force on axisymmetric rotating thin film flows. *Intl. J. Non-Linear Mech.* **36**, 629–635.

Needham, D. J. & Merkin, J. H. 1987 The development of nonlinear waves on the surface of a horizontally rotating thin liquid film. *J. Fluid Mech.* **184**, 357–379.

Rauscher, J. W., Kelly, R. E. & Cole, J. D. 1973 An asymptotic solution for the laminar flow of thin films on a rotating disk. *J. Appl. Mech.* **40**, 43–47.

Rifert, V. G., Barabash, P. A. & Muzhilko, A. A. 1982 Stochastic analysis of wave surface structure of liquid film flowing under centrifugal forces. *Izv. VUZov. Energetika* **(8)**, 62–66.

Shkadov, V. Ya. 1967 Wave flow regimes of a thin layer of viscous fluid subject to gravity. *Fluid Dyn.* **2** (1), 43–51.

Shkadov, V. Ya. 1973 *Some Methods and Problems of the Theory of Hydrodynamic Stability*. Scientific Proceedings 25. Institute of Mechanics of Lomonosov Moscow State University, Moscow.

Shkadov, V. Ya. 1977 Solitary waves in a viscous liquid layer. *Fluid Dyn.* **12** (1), 63–66.

Shkadov, V. Ya. & Sisoev, G. M. 2000 Wavy falling liquid films: theory and computation instead of physical experiment. In *IUTAM Symp. on Nonlinear Waves in Multi-Phase Flow* (ed. H.-C. Chang), pp. 1–10. Notre Dame University, Notre Dame, USA: Kluwer.

Shkadov, V. Ya. & Sisoev, G. M. 2001 On theory of solitary waves in falling layer of viscous liquid. *Phys.–Dokl.* **46** (10), 760–764.

Shvets, A. F., Portnov, L. P., Filippov, G. G. & Gorbunov, A. I. 1992 Flow of an axisymmetric film of viscous liquid on the surface of a spinning disc. *Theore. Found. Chem. Technol.* **26**, 895–900.

Sisoev, G. M., Matar, O. K. & Lawrence, C. J. 2003 Modelling of film flow over a spinning disk. *J. Chem. Technol. Biotechnol.* **78**, 151–155.

Sisoev, G. M. & Shkadov, V. Ya. 1987 Flow stability of a film of viscous liquid on the surface of a rotating disc. *J. Engng Phys.* **52**, 671–674.

Sisoev, G. M. & Shkadov, V. Ya. 1990 Helical waves in a liquid film on a rotating disc. *J. Engng Phys.* **58**, 573–577.

Sisoev, G. M. & Shkadov, V. Ya. 1997*a* Development of dominating waves from small disturbances in falling viscous-liquid films. *Fluid Dyn.* **32** (6), 784–792.

Sisoev, G. M. & Shkadov, V. Ya. 1997*b* Dominant waves in a viscous liquid flowing in a thin sheet. *Phys.–Dokl.* **42** (12), 683–686.

Sisoev, G. M. & Shkadov, V. Ya. 1999 On two-parametric manifold of the waves solutions of equation for falling film of viscous liquid. *Phys.–Dokl.* **44** (7), 454–459.

Sisoev, G. M., Tal'drik, A. F. & Shkadov, V. Ya. 1986 Flow of a viscous liquid film on the surface of a rotating disc. *J. Engng Phys.* **51** (4), 1171–1174.

Thomas, S., Faghri, A. & Hankey, W. 1991 Experimental analysis and flow visualization of a thin liquid film on a stationary and rotating disk. *Trans. ASME: J. Fluids Engng* **113** (1), 73–80.

Woods, W. P. 1995 The hydrodynamics of thin liquid films flowing over a rotating disc. PhD thesis, University of Newcastle upon Tyne, UK.